Planet Mercury: Volcanism in a theatre of global contraction, with examples from the Hokusai quadrangle

Journal of Volcanology and Geothermal Research xxx (xxxx) xxx

Contents lists available at ScienceDirect

Journal of Volcanology and Geothermal Research

journal homepage: www.elsevier.com/locate/jvolgeores

Planet Mercury: Volcanism in a theatre of global contraction, with examples from the Hokusai quadrangle

Jack Wright [a,*], Paul K. Byrne [b], David A. Rothery [a]

[a] School of Physical Sciences, The Open University, Walton Hall, Milton Keynes MK7 6AA, UK
[b] Planetary Research Group, Department of Marine, Earth, and Atmospheric Sciences, North Carolina State University, Raleigh, NC 27695, USA

ARTICLE INFO

Article history:
Received 30 July 2020
Received in revised form 24 May 2021
Accepted 2 June 2021
Available online xxxx

Keywords:
Mercury
Effusive volcanism
Explosive volcanism
Tectonism
Pitted ground

ABSTRACT

Mercury's geological history has been dominated by global contraction caused by secular cooling of the planet's interior. This cooling has had a profound effect on the expression of the planet's volcanism and tectonism, and the expressions of these two surface evolutionary processes are deeply intertwined. Here, we use case studies from the Hokusai quadrangle of Mercury to gain insight into the interplay between Mercury's volcanism and tectonism, which we review throughout this paper. We perform the first crater size–frequency analysis of the southernmost extent of Borealis Planitia, Mercury's largest expanse of volcanic plains, and find that it formed ~3.8–3.7 Ga. We discuss the importance of "intermediate plains", a widespread unit in the Hokusai quadrangle, as the manifestation of relatively low-volume effusions with an uncertain stratigraphic relationship with Borealis Planitia. Finally, we detail the formation of the Suge Facula pitted ground during the geological history of Rachmaninoff crater, and hypothesise that such textures probably formed more widely on Mercury but have often either been buried by thick lava flows or otherwise obscured. Unanswered questions in this work can be used to drive the next phase of Mercury exploration and research with the arrival of the BepiColombo mission.

1. Introduction

Results from the MErcury Surface, Space ENvironment, GEochemistry, and Ranging (MESSENGER) mission provided many answers about the history of volcanism on the Solar System's innermost planet, yet many questions remain. With the launch of the BepiColombo mission (Benkhoff et al., 2010; Rothery et al., 2020a), set to return data from Mercury from 2026, we are in an appropriate interval to review our understanding of the planet's volcanism, which is strongly tied to its global tectonic regime. Where appropriate, we illustrate the interplay between tectonism and volcanism on Mercury with case studies from the planet's Hokusai quadrangle (H05: Fig. 1: Wright et al., 2019), which encapsulates many aspects of the key constituent processes. For ease of comparison with Wright et al. (2019), in which the geological mapping of the quadrangle was presented, here we show several figures of the whole or parts of H05 in the same Lambert Conformal Conic (LCC) projection (central meridian, 45°E; standard parallels, 30°N and 58°N), which we refer to as the "default" LCC projection of H05.

1.1. Mercury data

After NASA's Mariner 10 (1974–1975: Dunne and Burgess, 1978), that same agency's MESSENGER mission (2008–2015: Solomon et al., 2018) is only the second spacecraft to have visited Mercury, and the first to have orbited the planet. Its Mercury Dual Imaging System (MDIS: Hawkins et al., 2007) instrument, which incorporated a monochrome narrow-angle camera (NAC) and a multispectral wide-angle camera (WAC), provided the first global image set of the planet's surface (Figs. 2 and 4). For thermal regulation, MESSENGER was placed in a highly elliptical polar orbit to radiate excess heat from the Sun and Mercury's dayside surface (Solomon et al., 2007). At closest approach altitudes of ~200 km over the northern hemisphere, the NAC captured images with ground resolutions of a few tens of meters per pixel. The small footprint of the NAC over the northern hemisphere was compensated for by the WAC's wider field of view. However, MESSENGER's higher altitude over the southern hemisphere resulted in reduced spatial measurement resolution and coverage for several instruments, including MDIS. MESSENGER's Mercury Laser Altimeter (MLA: Cavanaugh et al., 2007) was unable to return much useable data south of 20°N because of the greater range to the planet when this part of Mercury was in view. Consequently, MLA-derived digital elevation models (DEMs) are available only for the northern hemisphere (Zuber et al., 2012). However, it was possible to create a global 665 m/pixel DEM of Mercury using stereophotogrammetry (Becker

* Corresponding author.
E-mail address: jack.wright@open.ac.uk (J. Wright).

https://doi.org/10.1016/j.jvolgeores.2021.107300

Please cite this article as: J. Wright, P.K. Byrne and D.A. Rothery, Planet Mercury: Volcanism in a theatre of global contraction, with examples from the Hokusai quadran..., Journal of Volcanology and Geothermal Research, https://doi.org/10.1016/j.jvolgeores.2021.107300

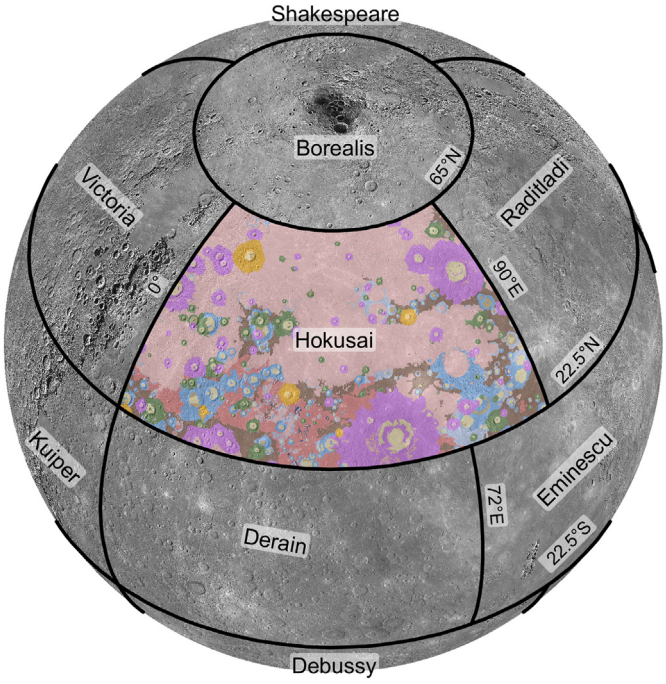

Fig. 1. Mapping quadrangles of Mercury. Mercury is divided into 15 quadrangles defined by latitude and longitude (examples shown here with black outlines; Davies et al., 1978). The Hokusai quadrangle is illustrated with the geological map of Wright et al. (2019). The base map is the 250 m/pixel MESSENGER MDIS mosaic in an orthographic projection, centered on 45°E, 45°N.

et al., 2016). Furthermore, Stark et al. (2017) produced a 222 m/pixel DEM for H05 from the superior resolution and viewing angle image data available for that quadrangle.

Often, the relative order of geological events can be readily discerned from MDIS images using the principle of superposition of proximal landforms and units (Fig. 2). Over greater distances, where features of interest are not in contact, their general state of landform degradation can be used as a qualitative proxy for relative age, such as for impact craters (Kinczyk et al., 2020). However, no rock samples from Mercury have been radiometrically dated, which means absolute dates for Mercury's geological units can be obtained only by measuring crater size–frequency distributions (CSFDs). This method relies on the assumption that planetary surfaces accumulated spatially random impact craters at expected rates over geological time (e.g., Neukum et al., 2001b). CSFDs for Mercury can be compared with those for the Moon, which have been calibrated with radiometrically dated samples, and absolute model ages can then be calculated for Mercury (by extrapolation of cratering rates and sizes between Mercury and the Moon: Neukum et al., 2001a). As a result, there is a high degree of uncertainty in the absolute model ages derived for Mercury; different ages can be determined from the same CSFD depending on the chronology (CF) and production functions (PF) used (e.g., Neukum et al., 2001b; Marchi et al., 2009; Le Feuvre and Wieczorek, 2011), which can make different assumptions about the impactor population and target physical properties. Alternatively, crater spatial densities can be compared without calculation of absolute model ages, by using $N(D)$ values, defined as the number, N, of craters equal to and greater than diameter, D, per some reference area (often, though not always, taken as 10^6 km^2). This approach yields *relative*, rather than model absolute, ages for units and landforms, which can in turn be compared with one another on the same body under the assumptions that the cratering flux and the mechanical response to impacting are similar.

Geological time on Mercury is divided into five time-stratigraphic systems: originally Kuiperian (~1 Ga–present), Mansurian (~3.5–1 Ga), Calorian (~3.9–3.5 Ga), Tolstojan (~4.0–3.9 Ga), and Pre-Tolstojan (>4.0 Ga: Spudis and Guest, 1988). However, absolute model ages for the beginnings of the Kuiperian and Mansurian stratigraphic systems were recently revised to ~280 Ma and ~ 1.7 Ga, respectively (Banks et al., 2017).

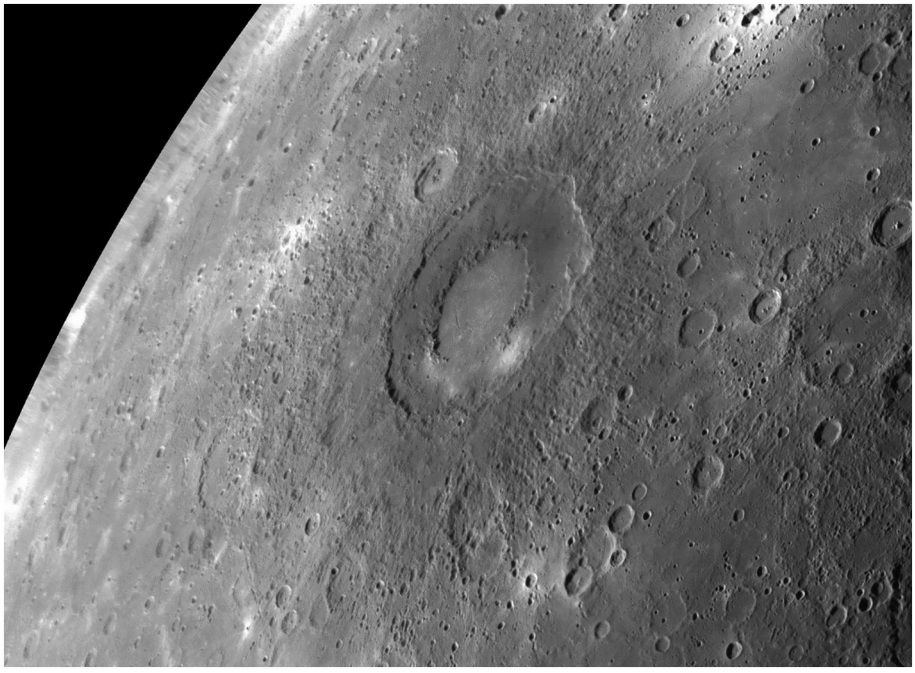

Fig. 2. An unprojected mosaic of MDIS NAC images captured during MESSENGER's third Mercury flyby. Southeast H05, which MESSENGER imaged for the first time. The 305 km-diameter peak ring impact basin named Rachmaninoff occupies the center of this view and is surrounded by its radially textured impact ejecta. Rachmaninoff ejecta superposes relatively uncratered "smooth plains" in the upper- and lower-right of this view, demonstrating that the Rachmaninoff impact postdates emplacement of the local smooth plains. Smooth plains within Rachmaninoff itself must either be contemporaneous with, or younger than, the impact. The spatial resolution of this mosaic approaches ~500 m/pixel toward the lower-right corner of this figure. Credit: NASA/Johns Hopkins University Applied Physics Laboratory/Carnegie Institute of Washington.

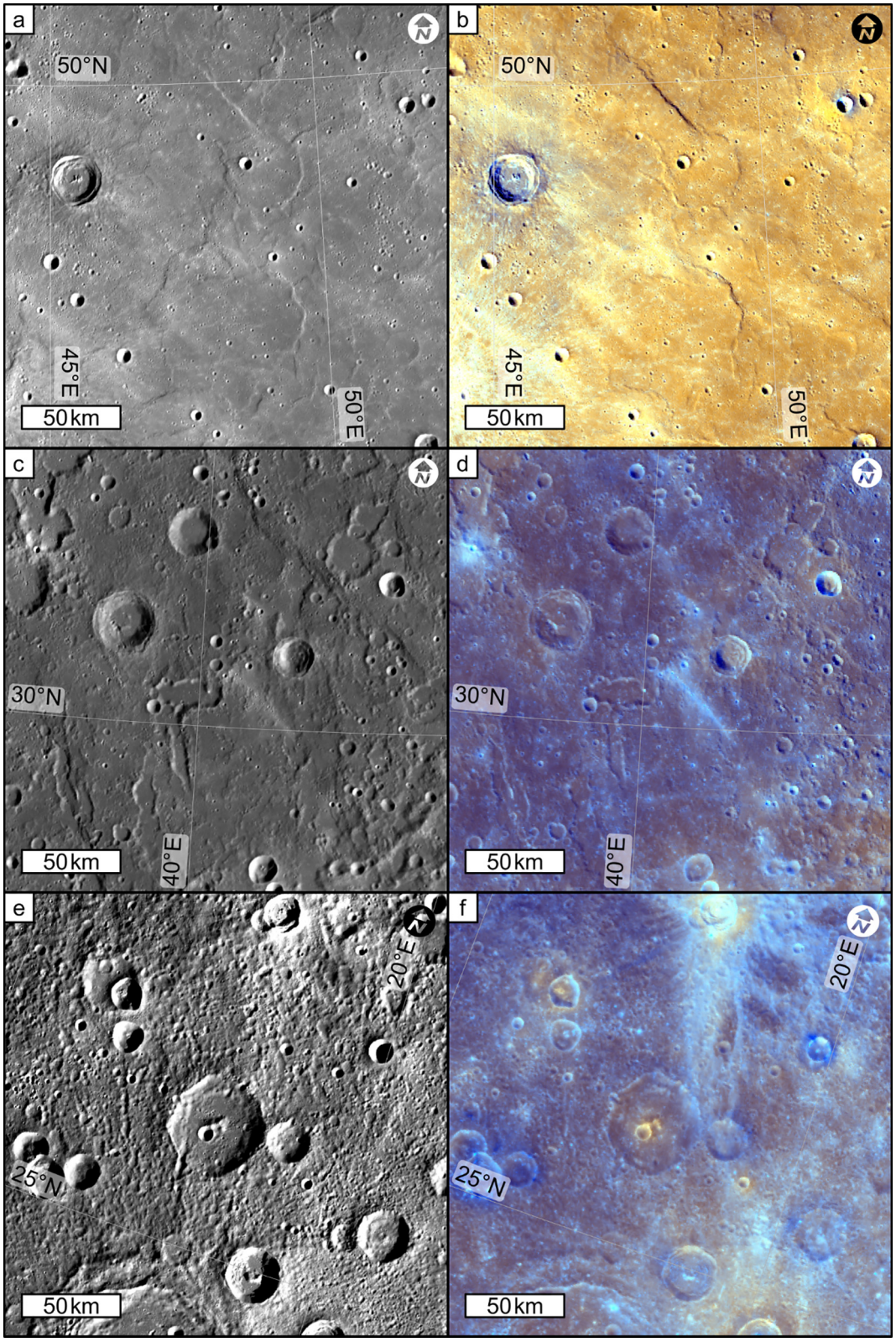

Fig. 3. Comparison of plains types on Mercury. (a,b) Smooth plains. (c,d) Intermediate plains. (e,f) Intercrater plains. Panels (a), (c), and (e) show ~166 m/pixel MDIS mosaics. Panels (b), (d), and (f) show the ~665 m/pixel MDIS enhanced color mosaic. All panels show the default LCC projection of H05.

1.2. Background: volcanism on Mercury

Mercury has a prolonged history of both effusive and explosive volcanism (Byrne et al., 2018b), concentrated largely within the first billion years of its planetary history but with a potentially long coda.

1.2.1. Effusive volcanism

Almost the entire crustal surface of the planet was produced volcanically, although thereafter it was intensely battered and fragmented, especially in older regions, by impacts. This volcanism is recorded by "plains" that have sustained different degrees of impact cratering since their emplacement (Fig. 3).

1.2.1.1. Smooth plains. Over 27% of Mercury surface is morphologically classified as "smooth plains" (Figs. 3a,b and 4: Denevi et al., 2013). These plains, chiefly characterized by their relatively smooth surfaces between impact craters, rather than impact craters themselves, are indicative of some form of planetary resurfacing. Plains volcanism, equivalent to lunar mare volcanism, was quickly postulated as the origin of the smooth plains on the basis of Mariner 10 observations (Murray et al., 1974), although an alternative origin as fluidized impact basin ejecta/melt was suggested (Wilhelms, 1976) by analogy with Apollo 16 results for the Cayley Formation on the Moon (Eggleton and Schaber, 1972). Some resurfacing by impact basin ejecta emplacement has undoubtedly occurred on Mercury, but the distributions and volumes of most smooth plains are incompatible with an ejecta origin. Except for the circum-Caloris plains, smooth plains are generally not found around impact basins that could have deposited the plains as ejecta as adjudged by superposition relations.

Photogeological evidence for a volcanic plains origin for most of Mercury's smooth plains includes: embayment relations (Fig. 5a); the presence of completely flooded "ghost craters" (Fig. 5b); and spectral contrasts between smooth plains and their surroundings (Fig. 5c). On the basis of such evidence, >65% of smooth plains on Mercury are confidently judged to be volcanic in origin (Denevi et al., 2013). However, no unambiguously volcanic features, such as flow units/fronts, source vents, or pāhoehoe/ʻaʻā lava surface textures, have been unequivocally identified within the smooth plains (Byrne et al., 2018b). Smooth plains have probably buried their source vents/fissures (although see Byrne et al. (2013) for one possible preserved example), as is often the case in expanses of basaltic lavas on Earth and other terrestrial bodies (such as large igneous provinces: Byrne et al., 2018b), and finer-scale textures on multi-billion-year-old lava flows will almost certainly have been destroyed by subsequent impacts and the associated development and dispersal of regolith. Mercury's regolith is perhaps 25–40 m thick on the smooth plains (Kreslavsky and Head, 2015), meaning the original lava textures are probably deeply buried or pulverized—factors that improved imaging resolution would not be able to overcome. Consequently, planetary geologists must rely on other observations when interpreting images of Mercury's surface.

Major smooth plains deposits on Mercury (Fig. 4) include: Borealis Planitia (formerly known as Mercury's "northern smooth plains" or the "northern volcanic plains": Head et al., 2011; Ostrach et al., 2015); Caloris Planitia (the smooth plains within the Caloris Basin, the largest well-preserved impact basin on Mercury: Murchie et al., 2008; Fassett et al., 2009), and the circum-Caloris smooth plains that almost entirely surround the basin rim (Denevi et al., 2013). As an example, Borealis Planitia, the largest contiguous area of smooth plains on Mercury, has an estimated minimum volume of 4×10^6 km^3 (Ostrach et al., 2015), which is comparable to the volume of the Siberian Traps large igneous province on Earth (Fedorenko et al., 2000).

These large smooth plains units all have similar CSFDs, which suggests that they formed during a relatively short window (Denevi et al., 2013; Ostrach et al., 2015; Fassett et al., 2009: Table 1). This conclusion is consistent with observations of several superposition relationships of opposite senses between the smooth plains interior and exterior to the Caloris Basin, indicating effectively contemporaneous emplacement (Rothery et al., 2017). Byrne et al. (2016) measured CSFDs of several smaller (though still expansive) smooth plains deposits, finding that most such distributions are similar to those of the more extensive smooth plains. These authors determined the smooth plains with the lowest $N(10)$ to have a value of 29 ± 21, to which they ascribed an

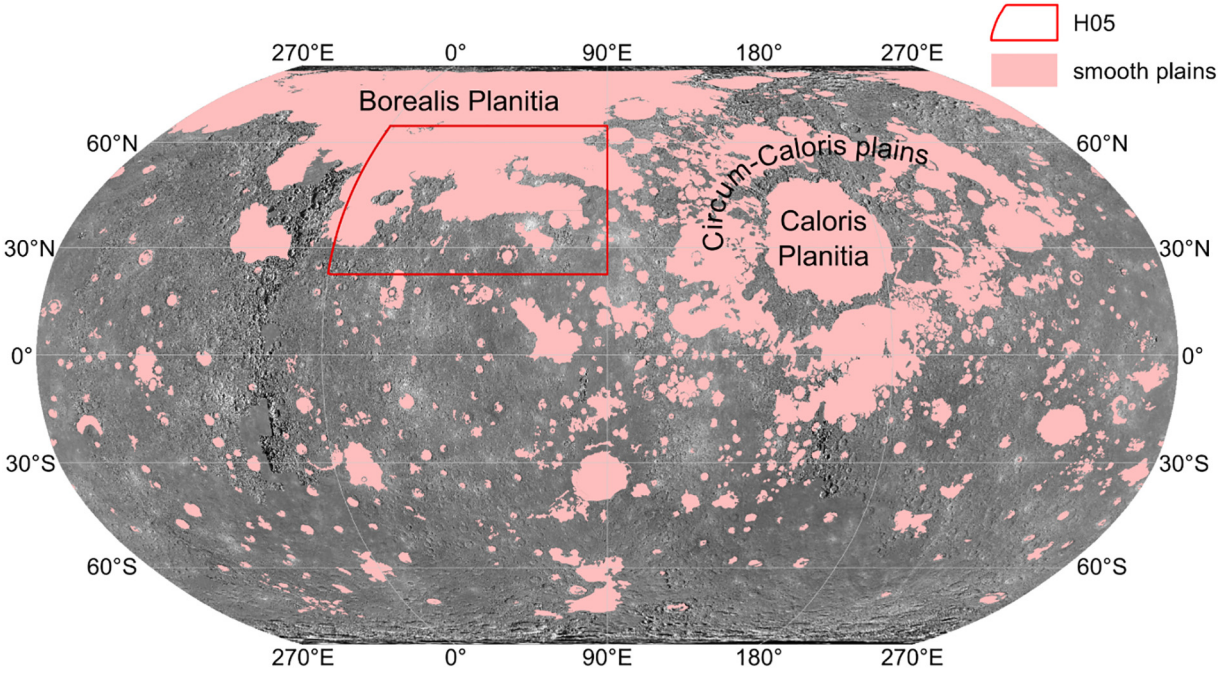

Fig. 4. Smooth plains on Mercury. The pink color indicates units mapped as smooth plains by Denevi et al. (2013) incorporating updates by those original authors (Byrne et al., 2018b). Smooth plains cover ~27% of Mercury's surface. Abundant, quasi-circular patches of smooth plains indicate deposits within impact craters in most cases, at least some of which are volcanic. H05 is outlined in red. This figure shows the MESSENGER 250 m/pixel global monochrome mosaic in a Robinson projection centered on Mercury's equator at 90°E.

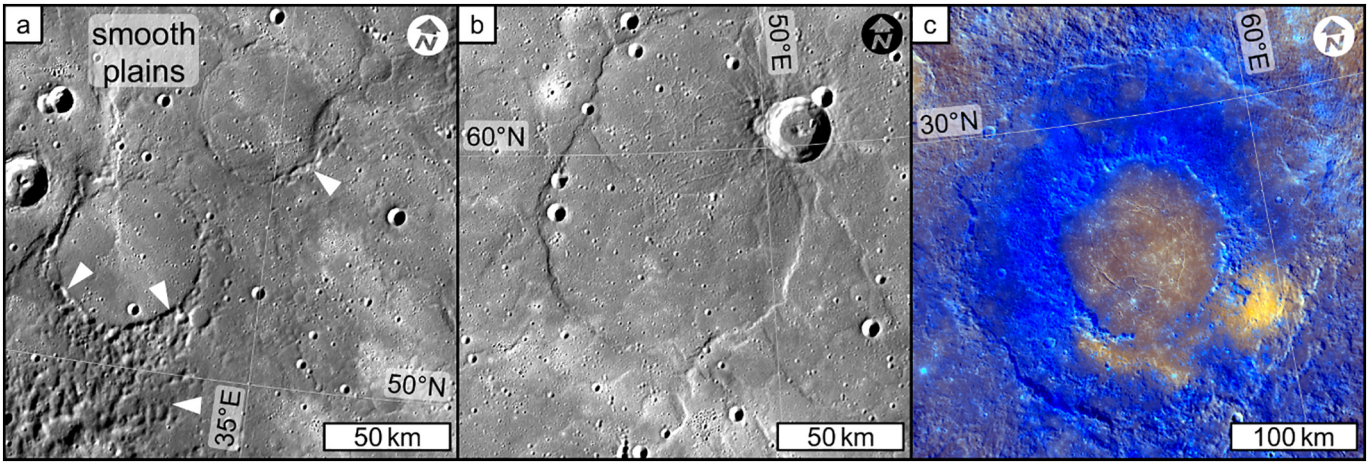

Fig. 5. Examples of evidence for a volcanic origin of Mercury's smooth plains in H05. (a) Smooth plains most commonly occur in locally low-lying regions and embay the surrounding terrain (white arrows), indicating that they were emplaced by infilling *after* the older, more rugged terrain had formed. (b) Rings of wrinkle ridges in the smooth plains indicate where pre-existing impact craters have been partially or entirely buried (forming "ghost craters"). Populations of larger and smaller ghost craters require multiple burial events separated by geological time to coexist closely. (c) When seen with enhanced color WAC images, smooth plains within Rachmaninoff crater are relatively high-reflectance and are spectrally red, and they have sharp color and geomorphic contacts with the surrounding low-reflectance, bluer, material on the crater floor. Panels (a) and (b) show ~166 m/pixel MDIS mosaics. Panel (c) shows the ~665 m/pixel MDIS enhanced color mosaic. All panels show the default LCC projection of H05.

Table 1
Published crater densities and absolute model ages for some extensive smooth plains deposits on Mercury. Footnotes indicate citations for the model production functions used to determine the absolute model ages shown.

Crater count area	Source	*N*(10)	Absolute model age (Ga)
Borealis Planitia	Ostrach et al. (2015)	67 ± 4	3.70 ± 0.01[a] 2.5 ± 0.3[b] ~2[c] ~3.7[d] 3.30 ± 0.3[e]
Caloris Planitia	Denevi et al. (2013)	80 ± 7	~3.7–3.9[f]
	Fassett et al. (2009)	75 ± 7	None given
Circum-Caloris smooth plains	Denevi et al. (2013)	92 ± 16	~3.7–3.9[f]

[a] Neukum et al. (2001b).
[b] Marchi et al. (2009).
[c] Le Feuvre and Wieczorek (2011) using non-porous target scaling only.
[d] Le Feuvre and Wieczorek (2011) using porous target scaling only.
[e] Le Feuvre and Wieczorek (2011) using a best-fit combination of porous and non-porous target scaling.
[f] Strom and Neukum (1988).

absolute model age of 3.5 Ga (see Byrne et al., 2016 for details and assumptions of impact crater production function and chronology). Younger model ages for smooth plains deposits have been reported elsewhere (Prockter et al., 2010; Fegan et al., 2017), but for much smaller, local deposits confined mostly to impact crater floors, rather than corresponding to regional-scale resurfacing. Therefore, it seems that large-volume effusive volcanism on Mercury ceased ~3.5 Ga (Byrne et al., 2016).

1.2.1.2. Intercrater plains. The most spatially extensive geological unit on Mercury is the "intercrater plains" (Trask and Guest, 1975), which covers >70% of the planet's surface (Denevi et al., 2013). Intercrater plains, originally described as "level to gently rolling ground between and around large craters and basins [with a] high density of superposed small craters in the size range 5–10 km" (Trask and Guest, 1975) are everywhere embayed by smooth plains and are more heavily cratered, although the amount of cratering varies substantially across Mercury. Superposition, as well as areal crater density, demonstrates that the intercrater plains are older than the smooth plains; most intercrater plains were emplaced between ~4.1 and ~3.8 Ga (Marchi et al., 2013).

Several lines of evidence support a volcanic origin for most of the intercrater plains. The widespread occurrence of intercrater plains across the planet (most of the uncolored portions of Fig. 4 are intercrater plains), and the lack of large impact basins that could have supplied the necessary volume of ejecta material to produce such plains, argue for a large igneous province-style plains emplacement. Furthermore, it has been shown that smooth plains can be modified by overlapping fields of secondary craters from two or more relatively young primary impacts into a morphological texture indistinguishable from intercrater plains (Whitten et al., 2014). This observation supports the conclusion that intercrater plains were originally emplaced similarly to smooth plains, but at an earlier stage in Mercury's history such that these older plains have become more heavily cratered.

As further corroboration of this view, CSFDs for the most densely cratered smooth plains overlap within error with CSFDs for the least densely cratered intercrater plains (Whitten et al., 2014; Byrne et al., 2016). Furthermore, that no surface appears to have an absolute model age greater than ~4.1 Ga suggests that there was intense, continual resurfacing early in Mercury's history (Marchi et al., 2013) driven by the more energetic planetary and space environment in the early Solar System. For example, young Mercury's volcanism would have been enhanced while the planet's interior was hotter, and more intense impact bombardment during this time might have facilitated or even induced additional volcanism (Ivanov and Melosh, 2003; Elkins-Tanton and Hager, 2005).

1.2.1.3. Lava composition. Compositional data for Mercury's surface have been measured as elemental abundances and ratios by MESSENGER's X-Ray Spectrometer (XRS: Schlemm et al., 2007) and Gamma-Ray and Neutron Spectrometer (GRNS: Goldsten et al., 2007). GRNS data show that Mercury's surface is generally Fe poor (1.9 ± 0.3 wt % globally: Evans et al., 2012) and XRS data show it to be S-rich (up to 4 wt%: Nittler et al., 2011), indicating a strongly reducing planetary interior (Zolotov et al., 2013). XRS data suggest an average surface Si abundance of 25 wt% (equivalent to ~54 wt% SiO_2: Nittler et al., 2011).

XRS data have been used to create major element ratio maps of Mg/Si, Al/Si, S/Si, Ca/Si, and Fe/Si (Weider et al., 2015; Nittler et al., 2020). These maps provide evidence for "geochemical terranes" on Mercury, which in some instances spatially coincide with morphological units (Weider et al., 2015). GRNS-derived maps of Na and K abundances

also broadly support the concept of geochemical terranes (Peplowski et al., 2012, 2014).

In general, smooth plains have lower Mg/Si and higher Al/Si than more heavily cratered terrains (Weider et al., 2012). However, there is geochemical variation within the smooth plains, consistent with compositionally heterogeneous mantle sources. For example, southern Borealis Planitia in H05 (see Fig. 9) has an intermediate Mg/Si ratio (0.3–0.6), whereas most of the rest of Borealis Planitia has a lower such ratio (<0.3: Weider et al., 2015). Poleward of 80°N, Borealis Planitia has the highest K abundance (~2000 ppm: Peplowski et al., 2012) and Na content (~5 wt%: Peplowski et al., 2014) on the planet, whereas alkali content of the intercrater plains is generally lower. These observations support an evolution from more ultramafic lavas forming the intercrater plains in Mercury's early eruptive history toward feldspar-dominated lavas by the time of smooth plains emplacement (Namur and Charlier, 2017).

The higher spatial resolution of XRS data over Borealis Planitia allowed for a bulk composition for these plains to be determined with a lowered prospect that the composition would be contaminated by XRS pixels crossing into adjacent terrains (Vander Kaaden and McCubbin, 2016). Vander Kaaden and McCubbin (2016) created artificial Borealis Planitia melts, using SiO_2, TiO_2, Al_2O_3, CrO, FeO, MgO, MnO, CaO, Na_2O, K_2O, and FeS in proportions consistent with XRS data (Nittler et al., 2011), and allowed those melts to crystalise under a variety of Mercury environmental conditions (oxygen fugacity = ~2–7 $\log_{10}$ units below the iron-wüstite buffer, pressure = 0.57–5 GPa, temperature = 1100–2000 °C: see Vander Kaaden and McCubbin (2016) for full details of their experiments). These authors' experiments show that Borealis Planitia lavas should contain Na-rich plagioclase, Mg-rich olivine, and low-Ca, low-Fe pyroxene with sulfides of Fe, Cr, Mn, Ti, Mg, and Ca. Thus, Vander Kaaden et al. (2017) determine that the smooth plains on Mercury have an alkali- and sulfide-rich boninite- or komatiite-like composition.

Such lavas have high eruption temperatures, with rheologies similar to Hawai'ian basalts (Sehlke and Whittington, 2015; Vander Kaaden et al., 2017), which is in turn consistent with observations of lava-eroded channels and kipukas on Mercury (Byrne et al., 2013). Such Mercurian lavas probably did not have ultra-low viscosities, however.

1.2.1.4. Constructs. Unlike the other silicate volcanic bodies in the Solar System (Earth, the Moon, Venus, Mars, and Io), there is little morphological evidence of constructional volcanic edifices on Mercury (Byrne, 2020). For example, Mercury has no giant volcanoes equivalent to the Tharsis Montes of Mars, Hawai'ian volcanoes on Earth, nor the myriad large shields that dot the surface of Venus.

Long-wavelength topographic undulations of Mercury's surface observed in MLA data (Zuber et al., 2012), such as Borealis Planitia's "northern rise" (Fig. 6), which impinges on H05, appear not to be large shields. There is no summit complex and the floors of some impact craters on the flanks of this rise are tilted away from the summit, which indicates at least some of the rise's topography was caused by updoming (Zuber et al., 2012), rather than shield-building. A lack of compositional or temporal distinction between the northern rise and the surrounding smooth plains is also difficult to reconcile with a shield volcanism origin. However, a positive free-air gravity anomaly centered on the rise could be consistent with uplift caused by crustal underplating (James, 2018).

Notably, there is little evidence on Mercury for even small volcanic constructs, which are otherwise abundant throughout the Solar System. A feature in Caloris Planitia was suggested to be a candidate shield volcano on the basis of concentric tones apparent on fly-by images, interpreted as being the result of a subtle topographic rise surrounding an irregular depression, thus regarded as a vent (Head et al., 2008). However, orbital topographic data show the rise to have flank slopes of only ~0.14° (Rothery et al., 2014), although the central depression is widely accepted as an explosive volcanic vent (which also explains the concentric tonal pattern: see Section 1.2.2). One global survey for small constructs found two candidate volcanoes, but could not be conclusive about their origin, volcanic or otherwise, based on the available MESSENGER image resolution (Wright et al., 2018). In any case, small volcanic edifices formed by effusive eruptions are rare if not entirely absent on Mercury, suggesting that some aspect of the planet's typical eruptive mode prohibited their formation (e.g., high effusion rates), that evidence for their existence has been efficiently erased by impacts, or both (Wright et al., 2018). Ultra-low-viscosity lavas, which might be expected to build constructs less efficiently, appear to be inconsistent with analog experimental (Sehlke and Whittington, 2015; Vander Kaaden and McCubbin, 2016) and petrological models (Vander Kaaden et al., 2017) of Mercury composition lavas.

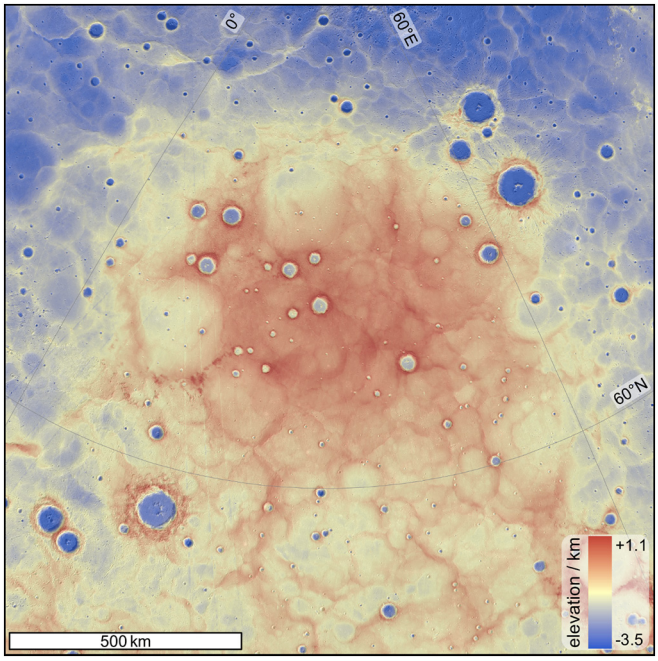

Fig. 6. Mercury's northern rise. The rise is situated within Borealis Planitia, the largest expanse of continuous smooth plains on Mercury. This figure is a portion of the 250 m/pixel MLA DEM overlain on the ~166 m/pixel MDIS mosaic in an orthographic projection centered on 33°E, 69°N.

1.2.2. Explosive volcanism

Being the innermost planet, Mercury was predicted to be depleted in volatile elements compared with the other rocky planets, because solar heating is expected to have driven volatiles out of that part of the protoplanetary disk (Wetherill, 1994). One of the most surprising results from the MESSENGER mission was that Mercury's surface is rich in many moderately volatile elements (Ebel and Stewart, 2018; Nittler et al., 2018). Consistent with this finding is the discovery of bright, diffuse spots that appear to be surficial materials draping topography and grading into their surroundings (Fig. 7a: Blewett et al., 2009). Most such deposits encompass one or several irregular pits near their mid-points, such as the example mentioned in the previous section. Such pits cannot be impact craters because of their non-circularity and lack of raised rims (Rothery et al., 2014).

Instead, these depressions are interpreted as explosively excavated volcanic craters, with their surrounding material having been deposited as ballistically emplaced pyroclasts (Kerber et al., 2009; Rothery et al., 2014; Jozwiak et al., 2018). In addition to their diffuse, gradational contacts with their surroundings (Fig. 7a,c), these deposits are characterized by high spectral reflectance and relatively steep slopes in plots of reflectance versus wavelength, making them relatively red compared with average terrains on Mercury. Originally, these deposits were informally numbered as "red spots" (Blewett et al., 2009), but are now

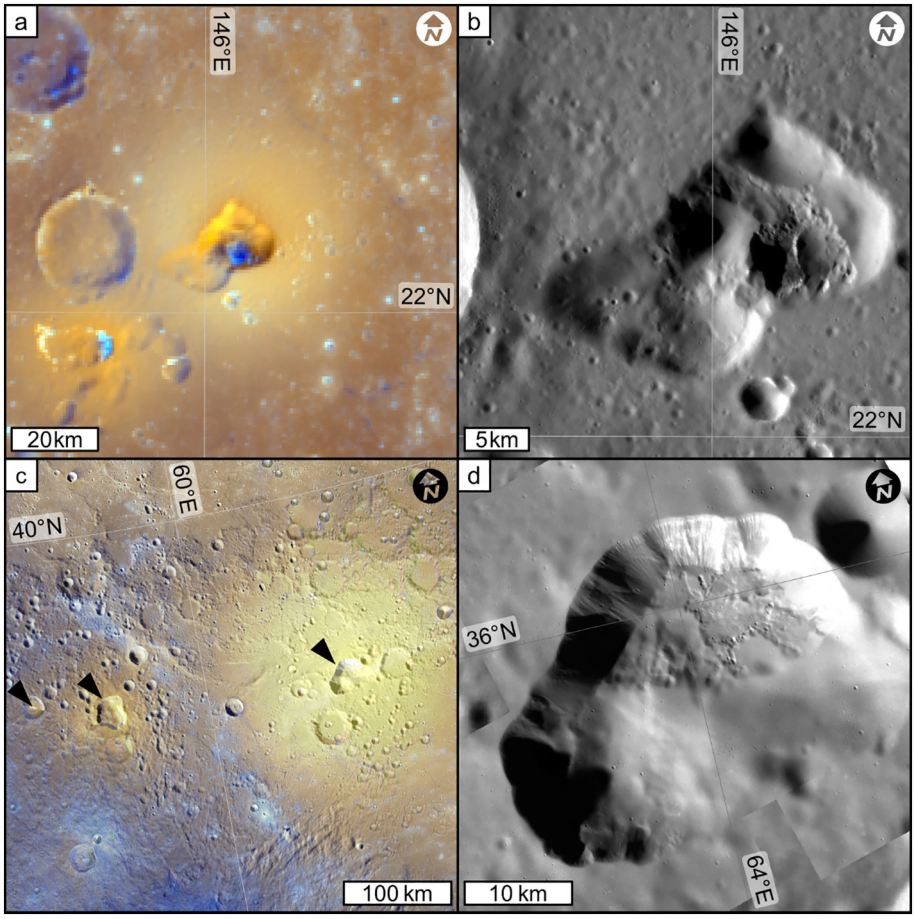

Fig. 7. Examples of putative explosive volcanism on Mercury. (a) An enhanced color (665 m/pixel) view of a pit in southwest Caloris Planitia. Agwo Facula is the relatively bright, circular, diffuse-edged deposit centered on the pit, and is interpreted as comprising ballistically emplaced volcanic ejecta erupted from the pit. This panel shows a stereographic projection centered on 146.3°E, 22.4°N. (b) MDIS NAC view of the Agwo Facula pit. The highly non-circular outline of the pit is strongly indicative of there having been multiple eruptions at this site. The pit has internal septa separating regions with different floor textures. This panel shows NAC image EN1015137802M (41.6 m/pixel) in a stereographic projection centered on 146.3°E, 22.4°N. (c) Enhanced color (665 m/pixel) view of three pits and their faculae in H05. The right arrow indicates the pit within Nathair Facula, the largest putative explosive volcanic deposit on Mercury. The middle arrow indicates the pit within Neidr Facula. The pit indicated by the left arrow is inside an even smaller unnamed facula. This panel is in the default LCC projection of H05, and the enhanced color mosaic is overlain on the 166 m/pixel MDIS monochrome mosaic. (d) MDIS NAC view of the pit within Nathair Facula. As with Agwo Facula's pit, it appears that the irregular outline of Nathair Facula's pit could not have been created by a single eruption (Rothery et al., 2020b; Pegg et al., 2021). Its variable floor texture freshness gives some indication of the migration of the eruption center (from southwest to northeast), but there are no cross-cutting septa to corroborate this hypothesis. This panel shows NAC images EN0224508427M, EN1003815055M, EN1003843856M, and EN1993843866M (~26 m/pixel) in the default LCC projection of H05.

known as "*faculae*" (sing. *"facula"*), the International Astronomical Union-approved descriptor term for "bright spot". The formally named examples have an individual name accompanied by the descriptor term *facula/faculae*.

On Earth, explosive volcanism is driven by the exsolution of volatile species from ascending magma (Cashman, 2004), and so surface observations of explosive volcanism on Mercury strongly suggest a source of volatiles within the planet's subsurface. Nearly 200 sites of putative explosive volcanism have been cataloged on Mercury (Kerber et al., 2011; Goudge et al., 2014; Thomas et al., 2014a; Jozwiak et al., 2018). Some examples have been studied in detail. For example, Agwo Facula (formerly "red spot 3"; Blewett et al., 2009; Kerber et al., 2011) is a 60 km-diameter deposit in southwest Caloris Planitia (which corresponds to the now-discounted constructional feature described in Section 1.2.1.4: Fig. 7a). The deposit is centered on an irregular pit interpreted as an explosively excavated volcanic crater (Head et al., 2008) that is >1 km deep (Rothery et al., 2014). Internal cross-cutting relationships of septa within the pit indicate that the pit constitutes at least nine overlapping volcanic vents, making the example within Agwo Facula a compound vent (Rothery et al., 2014). The shapes and mutual relationships between vents associated with each pit have no resemblance to the expected morphological results of subsidence along caldera-bounding ring faults, but are consistent with explosive excavation, likely modified by subsequent collapse into evacuated conduits. Recently, Pegg et al. (2021) showed that ~70% of explosive volcanic vents on Mercury are compound, so that multiple eruptions at each vent site are the norm—at least in those examples preserved on the surface.

Another important example is Nathair Facula (previously referred to informally as NE Rachmaninoff: e.g., Kerber et al., 2011; Weider et al., 2016), which is the largest putative pyroclastic deposit on Mercury (~140 km in radius; Fig. 7c). Indeed, Nathair Facula hosts the planet's largest vent (which is 31 km across). Kerber et al. (2011) determined that a substantial enrichment in magmatic volatiles would be required for erupted material to achieve the minimum ejection velocity to transport pyroclasts to the observed edge of the deposit. MESSENGER XRS data show a depletion of S in Nathair Facula compared with its surroundings (Weider et al., 2016). Similarly, MESSENGER NS data suggest that C is 1–2 wt% less abundant in Nathair Facula than in its surroundings (Peplowski et al., 2016).

Under the strongly reducing conditions of Mercury's interior (McCubbin et al., 2012), S should be soluble in magma. Weider et al. (2016) suggested that S and C depletions at Nathair Facula were caused by the oxidation of magma-soluble S and C by oxides, such as SiO_2 and

FeO, to form volatile species such as SO_2 and CO. These S- and C-bearing oxides might have volatilized in the magma, driven the explosive eruptions that formed Nathair Facula and subsequently been lost to space, thus leaving a reduced spectral signature for S and C in the Nathair Facula deposit. Furthermore, the loss of C that was previously in the form of graphite, held to be an important darkening agent stable at Mercury's surface (Peplowski et al., 2016), could help to explain the relatively high spectral reflectance of Nathair Facula and other putative pyroclastic deposits (Weider et al., 2016).

As with effusive volcanism, there is no evidence for pyroclastic constructs beyond subtle slopes associated with some faculae, which, as surficial deposits, are generally too thin to hide pre-existing impact craters (Rothery et al., 2014; Thomas et al., 2014b). Numerical simulations under Mercury surface conditions (i.e., a vacuum, and surface gravity of 3.7 ms^{-2}) suggest that pyroclastic cones, such as those found on Earth (e.g., Riedel et al., 2003), and interpreted to have formed on the Moon (e.g. Lawrence et al., 2013) and Mars (e.g., Brož and Hauber, 2012), cannot form to dimensions that are observable with present data (Brož et al., 2018).

Faculae superpose the smooth plains of Caloris Planitia (Head et al., 2008; Rothery et al., 2014), indicating that explosive volcanism locally outlasted effusive volcanism. There have been no observations of smooth plains embaying a facula anywhere on Mercury. This observation suggests that explosive volcanism generally outlasted effusive volcanism on Mercury, with the possible exception of highly localized, post-impact, late-stage effusive volcanism (Prockter et al., 2010; Chapman et al., 2012). Although large-volume effusive volcanism appears to have ceased ~3.5 Ga (Byrne et al., 2016), candidate pyroclastic vents have been observed within craters that retain bright albedo rays (Thomas et al., 2014a; Jozwiak et al., 2018). Ray-bearing craters have a size-frequency distribution consistent with them having formed between 280 ± 60 Ma and the present day (Banks et al., 2017), which means explosive volcanism potential persisted into Mercury's most recent geological history. Of note, there is no geological evidence preserved on Mercury to indicate either way whether explosive eruptions occurred *during* the phase of major effusive activity. Landform assemblages associated with explosive volcanism on Mercury appear to be better preserved than those expected of effusive volcanism (e.g. source vents/fissures, flow fields) because explosive volcanism persisted beyond ~3.5 Ga, when burial of pits and faculae by plains became unlikely and impact erosion was less efficient.

1.3. Background: global contraction on Mercury

The dominant form of tectonic deformation on Mercury is crustal shortening. The most prominent expression of that deformation is the planet's population of "lobate scarps" (Fig. 8). Although interpreted as the surface manifestations of thrust faults based on Mariner 10 observations (Murray et al., 1974), it was not until MESSENGER that their global ubiquity was revealed (Byrne et al., 2014). By analogy with Earth, these structures are displacement gradient folds, and likely fault-propagation folds, such that the landforms termed "lobate scarps" (which is not a geological term: Klimczak et al., 2019) are hanging-wall anticlines atop blind or surface-breaking thrusts.

Extensional tectonics are not nearly so prevalent on Mercury, and are overwhelmingly restricted to volcanically infilled impact features (Byrne et al., 2018a). Patterns in thrust orientation and spatial density may be controlled by some combination of tidal despinning (Melosh and Dzurisin, 1978; Dombard and Hauck, 2008), crustal thickness variations (Galluzzi et al., 2019), and thermal differences (Beuthe, 2010), but the overall horizontally compressive stress regime that brought about global thrust faulting was probably caused in the main by secular cooling of the planet's interior and the consequent global contraction (Byrne et al., 2016). Secular cooling and global contraction have been predicted to have a strong influence on the volcanic evolution of single-plate planets (Solomon, 1978).

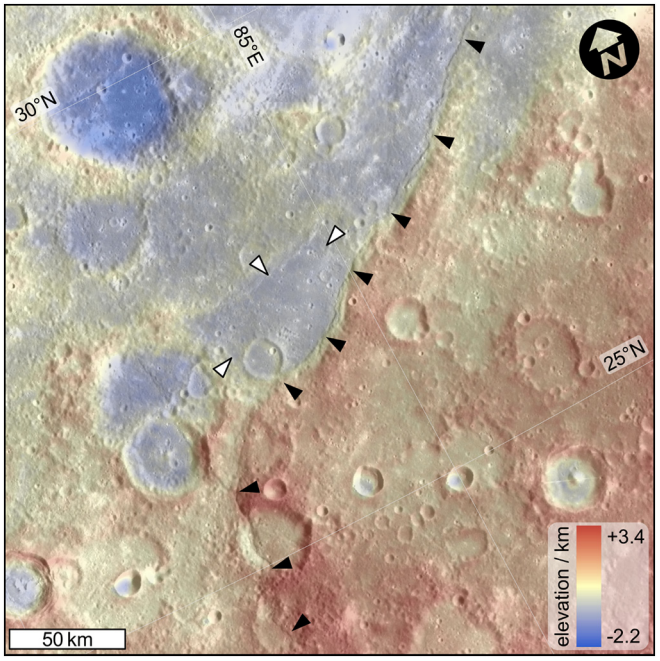

Fig. 8. Unity Rupes, an example of a lobate scarp in H05. This figure shows the 222 m/pixel stereo-derived DEM (Stark et al., 2017) overlain on the ~166 m/pixel MDIS monochrome mosaic in the default LCC projection of H05. Lobate scarps, such as Unity Rupes, are probably the surface manifestations of thrust faults. Black arrows are placed on the upthrown side of the fault and point at the fault surface break. White arrows indicate a small, ponded patch of smooth plains in front of Unity Rupes (see Section 2.3.2).

Several studies have investigated the onset, duration, and cessation of lobate scarp activity. Banks et al. (2015) examined the superposition relationships between impact craters in various states of degradation along the lengths of several lobate scarps. Crater degradation was used as a proxy for crater age (Kinczyk et al., 2020), and craters with certain characteristics of degradation (e.g. the presence or absence of bright crater rays, preserved terraces, and central peak, etc.) have been used to update absolute model ages for the time-stratigraphic systems on Mercury (Banks et al., 2017). A lobate scarp segment that cuts a crater must have undergone at least some of its total fault movement after the formation of that crater (Banks et al., 2015). In such a case, it is difficult to know how much fault displacement, if any, occurred before the impact crater formed or how much time passed between crater formation and the latest increment of slip occurring. Therefore, the age of the cross-cut impact crater (inferred from its degradation classification) *qualitatively* offers a maximum age for the last slip event of the cross-cutting segment of a lobate scarp.

Conversely, a lobate scarp segment that is superposed by an impact crater indicates that resolvable movement on the superposed scarp segment ceased before that crater formed (Banks et al., 2015). In this case, it is difficult to know how much time passed between the cessation of faulting and the formation of the impact crater. Therefore, the age of the superposing impact crater *qualitatively* provides a minimum age for the local cessation of fault activity (Banks et al., 2015). Based on their observations of impact crater–lobate scarp superposition relationships, Banks et al. (2015) inferred that the surface manifestation of global contraction had initiated at the time of the Calorian system (~3.9 Ga). Some lobate scarp segments superpose Mansurian and Kuiperian craters, indicating that at least some faulting locally continued through these periods (Banks et al., 2015).

Buffered crater statistics have been used to estimate absolute model ages for several of the largest lobate scarp systems on Mercury (Giacomini et al., 2015, 2020). These studies estimate that activity on the largest lobate scarps ceased at around ~3.8–3.6 Ga. Very small, fresh lobate scarps suggest that new scarp formation continued at

least until Mercury's recent geological past, and might be ongoing today (Watters et al., 2016), although there so far has been no substantive assessment of how these smaller, fresh scarps are kinematically linked to the older, larger scarps across Mercury.

2. Interplay between tectonism and volcanism on Mercury

2.1. Influence of Mercury's tectonics on timing of effusive volcanism

The most important influence of Mercury's tectonic regime on its volcanism is the apparent cessation of large-volume effusions ~3.5 Ga. Secular cooling of the planet's interior led to global contraction, which induced a global horizontally compressive stress regime in the lithosphere (Solomon, 1978; Byrne et al., 2016), evidenced by a global distribution of thrust fault-related landforms superposing volcanic plains (Byrne et al., 2014). Horizontally compressive stresses in the lithosphere inhibit magma ascent when they exceed the ability of magma to keep a conduit open (Byrne, 2020). This condition favors lateral magma transport within subsurface sills, rather than dyke propagation to the surface (Menand et al., 2010). The cessation of large-volume effusive volcanism in response to global contraction, which seems to have occurred on the Moon as well (Solomon and Head, 1980), appears to have been geologically abrupt on Mercury, as shown by the clustering of smooth plains absolute model ages 3.5–3.7 Ga (Byrne et al., 2016).

Here, we report for the first time new CSFDs for that portion of Borealis Planitia situated within H05, which corroborate this trend. We acquired crater statistics for our mapped original extent of the Borealis Planitia smooth plains within H05 (Fig. 9). We counted all craters >5 km in diameter that superpose the plains (e.g. crater ejecta/rim unembayed by the plains: Wright et al., 2019), but we base our interpretations mainly on craters ≥10 km in diameter to avoid including secondary impact craters. Primary impact craters form when a space object impacts a planetary body at hypervelocity. Material ejected from primary craters can in turn impact the planetary surface and form secondary craters, which can be as large as ~10 km in diameter on Mercury, because of the high average primary impact velocity (Strom et al., 2008; Byrne et al., 2016). If such secondary craters were included in the crater count, they would alter the crater size-frequency distribution of the surface being counted, which could return an incorrectly old age, or the distribution might not fit on an isochron at all. We also divided Borealis Planitia within H05 into three spectrally distinct subregions—north (relatively spectrally red), southwest (relatively blue), and southeast (relatively red)—to test if these spectral reflectance differences correspond to different CSFDs that might indicate lavas of varying ages and/or compositions. Our calculated $N(10)$ values for Borealis Planitia within H05 (Table 2) agree well with those determined by Ostrach et al. (2015) for Borealis Planitia north of 50°N (Table 1).

We plotted cumulative frequency plots for our crater counts using CraterStats2 (Fig. 10). We derived all absolute model ages using the production and chronology functions (for porous scaling) of Le Feuvre and Wieczorek (2011). We have plotted isochrons for absolute model ages with two decimal places to highlight different crater size-frequency populations—but consider only the first two figures of these ages to be significant. Broadly, these plots show that the uppermost smooth plains of Borealis Planitia within H05 have absolute model ages of ~3.7–3.8 Ga, consistent with previous measurements (Ostrach et al., 2015). The overall Borealis Planitia cumulative frequency curve does not plot on a single isochron, indicative of more than one crater population preserved here.

Specifically, craters >40 km in diameter plot approximately on the 3.8 Ga isochron, whereas craters below this diameter threshold plot beneath this isochron. This finding means that the smooth plains within H05 either have a surplus of craters >40 km in diameter or are deficient in craters <40 km in diameter. A surplus of craters >40 km in diameter could be explained by the inclusion in our counts of large craters that were buried by (and thus predate) the smooth plains. This possibility is not likely, since Wright et al. (2019) mapped the ejecta of craters >20 km in diameter, and such ejecta is resolvably embayed by smooth

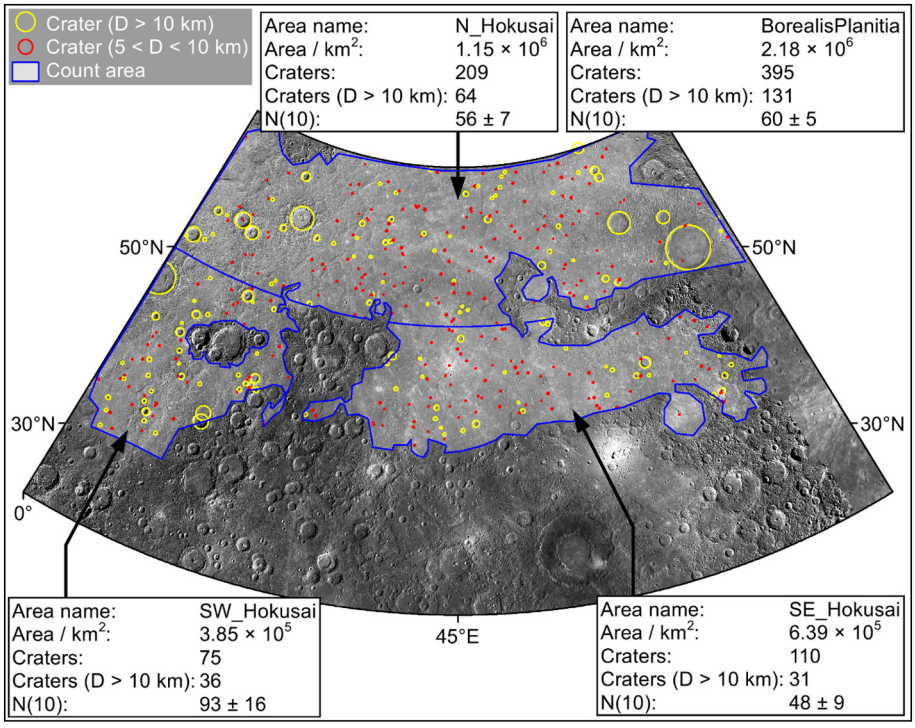

Fig. 9. Craters and count areas of smooth plains in H05. That portion of Borealis Planitia within H05 is divided into three labelled (black arrows) count regions. For each region, the area, total number of counted craters, number of craters >10 km in diameter, and calculated $N(10)$ values are shown. Additionally, we show aggregate crater statistics for all three count regions in the upper right of the figure. Craters and count areas are overlain on the ~166 m/pixel MDIS monochrome mosaic shown in the default LCC projection of H05.

Table 2
Summary table of H05 crater size–frequency analyses from this study.

Crater count area	$N(10)$	Absolute model age (Ga)[a]
Borealis Planitia	60 ± 5	3.7–3.8
North Hokusai	56 ± 7	3.7–3.8
Southwest Hokusai	93 ± 16	3.7–3.8
Southeast Hokusai	48 ± 9	3.7

[a] Estimated using the model production function of Le Feuvre and Wieczorek (2011) with porous target scaling.

plains in many cases; thus, it is straightforward to identify those large craters superposed by and thus older than these smooth plains.

A deficit of craters <40 km in diameter could be explained by a partial resurfacing event within Borealis Planitia, which preferentially hid such craters. Two candidate partial resurfacing mechanisms applicable to H05 include by lavas of limited spatial extent, or by ejecta from large craters superposing the smooth plains. Multiple resurfacing events within Borealis Planitia are already evidenced by its closely collocated populations of large and small ghost craters (Ostrach et al., 2015). Young, large craters such as Rustaveli, Sousa, and the Hokusai crater

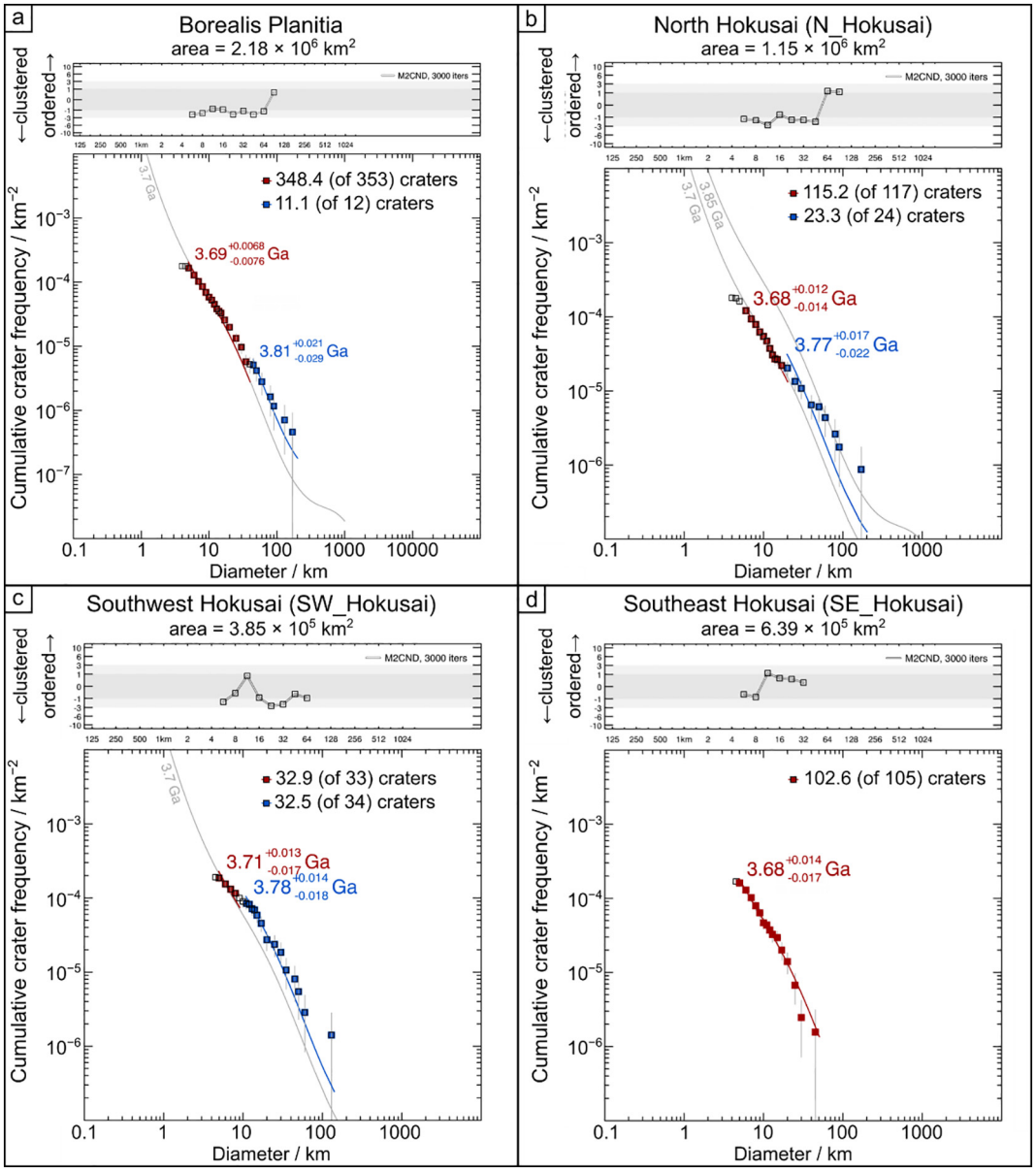

Fig. 10. Crater size–frequency plots for the Borealis Planitia count areas in H05. . CSFDs of Borealis Planitia in H05 (a), and northern (b), southwestern (c), and southeastern (d) subdivisions of Borealis Planitia in H05. In each panel, the cumulative crater size-frequency plot is shown (bottom) alongside its corresponding crater spatial randomness plot (top). In these cumulative frequency plots, each point represents the number of impact craters per square kilometer in the count area (N_{cum}) of equal or greater diameter (D) to the bin indicated on the x-axis. Error bars (the vertical gray lines) are given by $\pm\frac{1}{Area}[N_{cum}(D)]^{1/2}$ (Michael and Neukum, 2010). Isochrons (gray curves), which represent the shapes of ideal CSFDs of the labelled absolute age, are plotted for reference. All absolute model ages were calculated using the chronology and production functions of Le Feuvre and Wieczorek (2011) with porous target material scaling to reflect Mercury's fractured megaregolith. Craters <5 km in diameter were not used for fitting isochrons because our counts are not complete below this diameter threshold. The CSFDs shown in panels (a–c) do not lie along a single isochron (red and blue components), perhaps indicating a resurfacing event(s) that preferentially removed craters below a certain diameter (see text). Points on the spatial randomness plots show on the y-axis the number of standard deviations by which the mean second-closest neighbour distance (M2CND) of 3000 simulated impact crater populations deviates from the M2CND of the measured impact crater population at a given crater diameter (x-axis). In all cases, the M2CNDs plot within the gray bands, indicating that these values suggest the crater populations are spatially random, rather than ordered or clustered formations indicative of secondary cratering (Michael et al., 2012).

itself, which have extensive ejecta blankets draped atop Borealis Planitia, conceivably buried many craters superposing the smooth plains such that we could not recognise and so include them in our counts.

The cumulative frequency curves for northern and southwestern H05 also plot on two isochrons corresponding to ~3.7–3.8 Ga, which suggests that these regions contain the partial resurfacing event(s) that manifest in the CSFD of the whole of Borealis Planitia in H05. Conversely, the southeastern H05 count area cumulative frequency curve plots on a single isochron of ~3.7 Ga, suggesting that this is a chronostratigraphically homogeneous region at the scale of our crater count (craters >5 km in diameter). This result suggests that the best estimate absolute model age for the smooth plains of Borealis Planitia in H05 is ~3.7 Ga, a finding consistent with that of the entire Borealis smooth plains unit (Ostrach et al., 2015).

There are smooth plains in H05 that are stratigraphically younger than Mercury's major regions of smooth plains, but these are relatively minor volumes and they are generally restricted to impact crater interiors (Wright et al., 2016; Byrne et al., 2018b). Impact cratering results in several temporary and permanent effects on a planetary surface that are conducive to the extraction of melt from within the planet. The temporary effects include the deposition of heat (Davison et al., 2012) and, in the case of Mercury, the resetting of the global horizontally compressive stress regime at least within the crater (Byrne, 2020). More long-lived consequences of impacts pertinent to melt extraction include the opening of fractures as favourable magma ascent pathways (Klimczak, 2015), and the removal of overburden (i.e. crust and perhaps mantle: Byrne, 2020). It has been suggested that impacts can induce mantle decompression melting directly on Earth (Elkins-Tanton and Hager, 2005), but this mechanism seems unlikely on Mercury given its smaller size (i.e. its interior is cooler than Earth's at any given time) and the rarity of impact basins of the size required to generate sufficient decompression (>300 km-diameter) younger than 3.5 Ga (Ivanov and Melosh, 2003).

It would be useful to know for what period of time impact craters facilitated late-stage effusive volcanism after ~3.5 Ga. The small areal extents of smooth plains that are stratigraphically younger than their more extensive counterparts are generally insufficiently large for statistically robust CSFDs, making estimating their absolute model ages difficult. The best example of stratigraphically young smooth plains is within Rachmaninoff crater (Figs. 2 and 5c), which superposes, and thus postdates, Borealis Planitia (~3.7 Ga). Based on its relatively fresh geomorphology, Rachmaninoff probably formed around the transition between Mercury's Calorian and Mansurian systems (Banks et al., 2017; Wright et al., 2019; Kinczyk et al., 2020). Smooth plains within Rachmaninoff that bury parts of the peak ring suggest a depth (and hence volume) too great to be impact melt, and, furthermore, these plains are of a color supportive of their being volcanic, rather than impact melt (Prockter et al., 2010; Chapman et al., 2012). Depending on the timing of the formation of the Rachmaninoff basin, this suggests that impact craters could facilitate late-stage effusions on Mercury for at least a few hundred million years following the formation of the bulk of Borealis Planitia, and, by extension, the other lava units on the planet.

2.2. Influence of tectonism on Mercury's expression of volcanism

As global contraction caused large-volume effusive volcanism to wane, the decrease in eruptive volumes compared with the larger regions of smooth plains led to different morphological expressions of plains volcanism on Mercury. As described earlier, Mercury has two plains units of global import: smooth plains and intercrater plains (Denevi et al., 2013; Whitten et al., 2014). However, several quadrangle geological mappers (Galluzzi et al., 2016; Mancinelli et al., 2016; Guzzetta et al., 2017; Wright et al., 2019) have found photogeological textures that are notable at the quadrangle scale but that are *not* adequately described by the unit definitions of either smooth plains or intercrater plains, which are terms developed first from hemisphere- and then from global-scale mapping.

For example, Wright et al. (2019) dubbed a surface texture in H05 as "intermediate plains," describing the unit as "plains with a roughness intermediate between intercrater and smooth plains" and "hummocky terrain composed of degraded crater rims with intervening low-lying regions with smooth, level surfaces". Crucially, Wright et al. (2019) found that "smooth patches constitute ~50% of intermediate plains", meaning by definition that these units cannot be classified as intercrater plains (Whitten et al., 2014). However, at the quadrangle map scale, these intervening smooth patches were generally too finely interspersed with upstanding crater rims to be mapped as smooth plains and meaningfully displayed at the intended publication scale, which led Wright et al. (2019) to classify the intervening rough and smooth textures into "intermediate plains".

Wright et al. (2019) interpreted these "intermediate plains" as intercrater plains that have been partially inundated by smooth plains materials. This interpretation is supported by the presence of putative volcanic vents within regions mapped as intermediate plains in H05, indicating that a magma source was present beneath these regions. The same interpretation was made by Byrne et al. (2013) for what those authors termed "graded terrain" adjacent to several valleys filled with smooth plains northwest of the Caloris basin. This graded terrain has a muted topographic expression that transitions to the characteristic rugged texture of the intercrater plains with increasing distance from the valleys filled with smooth plains, interpreted as lava-modified channels (Byrne et al., 2013). These authors interpreted their graded terrain as evidence that at least some volume of erupted lavas within the region were not channelized but instead overbanked the channels to spread out over the surroundings. The "grading" of the muted intercrater plains into normal intercrater plains with increasing distance from the broad channels suggests that, as the lava flux in the region dropped, overland lava flow retreated until it became channel-confined once more.

It is possible that the intermediate plains in H05 could have formed in a similar manner: H05's intermediate plains are in contact with the smooth plains of Borealis Planitia, so the smooth patches within the intermediate plains could represent overland effusions that retreated before they were able to completely resurface the underlying intercrater plains. This hypothesis implies that the smooth patches within the intermediate plains are contemporaneous with or older than at least some of the smooth plains of Borealis Planitia. Alternatively, the smooth patches within the intermediate plains could represent terminal smooth plains volcanism, which could make them stratigraphically younger than the smooth plains of Borealis Planitia.

It is difficult to tell whether the effusions that formed the intermediate plains in H05 occurred in either the early or late stages of smooth plains emplacement in Borealis Planitia. If the interpretation of the intermediate plains as intercrater plains with a thin infilling of superposing lavas is correct, then age dating by measuring the CSFDs of the intermediate plains would be equivocal, since it would be difficult in many cases to determine if a crater superposes the intermediate plains or is a flooded/buried crater protruding from the underlying intercrater plains. Furthermore, the count areas for the smooth patches in the intermediate plains would be too small, and thus the number of included craters too low, to yield robust crater statistics. MESSENGER data are of insufficient resolution to determine this stratigraphic relationship unequivocally, and so this issue cannot be resolved until data from BepiColombo are returned.

2.3. Influence of tectonism on location of volcanism

2.3.1. Impact craters and basins

Impacts remove overburden, propagate fractures, deposit heat, and temporarily reset the local stress regime: all of these facilitate the extraction of magma to the surface (Byrne, 2020), thus impacts can

modulate the strong influence of Mercury's global horizontally compressive stress regime. Whatever the link between impact-generated heat and partial melting, it is clear that smooth plains, most of which are volcanic, commonly occupy impact structures (e.g., Head et al., 2008: Fig. 4). In H05, the Rachmaninoff and Rustaveli craters are instructive examples (Fig. 11). Ejecta from both these craters superposes smooth plains, which means that both craters probably postdate the cessation of large-volume effusive volcanism in this region.

The color contrast between the spectrally "red" interior Rachmaninoff smooth plains and the low-reflectance, blue material excavated in the crater's peak ring, rim, and intervening floor (Fig. 11a) suggests that there is a compositional difference between these regions. Impact melt generally does not have a spectral contrast with other crater materials, as the former is essentially a melted and resolidified form of the latter. No differentiation of melt sheets on Mercury by fractional crystallization has been observed. The smooth plains within Rachmaninoff embay the peak ring, rather than drape it, indicative of effusive emplacement by relatively low-viscosity lavas. Crater size–frequency studies of the Rachmaninoff interior plains suggest that these plains have a younger crater retention age than the crater's other materials. This finding strongly suggests that the interior plains were emplaced following an interval of geological time after the impact, which also argues against an impact melt origin for the plains (Prockter et al., 2010; Chapman et al., 2012).

"Pitted ground", present in the form of Suge Facula in southeast Rachmaninoff and other minor faculae south of the Rachmaninoff peak ring, has been suggested to have formed when lavas flowed over volatile-bearing substrates on Mercury (Thomas et al., 2014c). The pitted ground surface texture consists of clustered and coalesced pits tens of meters deep with uneven floors and muted rims (Thomas et al., 2014c). Pitted ground is generally surround by a reddish halo, similar to a facula associated with a large central pit, but the multitudinous pits of pitted ground are more consistent with near-surface volatilization, similar to tuff ring formation on Earth (Lorenz, 1986), rather than deep-seated volcanic eruptions. North of Suge Facula, the crater floor between the peak ring and the crater rim is spectrally low in reflectance and is blue, which implies that no smooth plains volcanic materials have reached there. We interpret Suge Facula and the other faculae in Rachmaninoff with the pitted ground texture as the most distal reaches of centrally sourced lava flows in the crater. Under this interpretation, the thickness of the lava diminishes toward the eastern extent of Suge Facula.

For a model in which pitted ground formed when lava flowed over a volatile-bearing substrate, the lava must have been of some specific thickness such that explosive loss of volatiles in the subsurface created pits at the surface. Furthermore, for the pitted ground texture to be present today, it must not have been buried too deeply by subsequent lava flows and/or obliterated by impact gardening. Therefore, the eastern spatial extent of Suge Facula was controlled either by lava flow length or by the presence of sufficient volatiles in the substrate (i.e., pitted ground will have formed only where flowing lava and volatile-bearing substrates coincided). Given that no spectrally "red" smooth plains are identified beyond Suge Facula, it appears that the extent and thickness of the lava controls the extent of Suge Facula, and that the eastern margin of Suge Facula is the approximate location of the flow terminus.

Although the western extent of Suge Facula might simply correspond to the boundary of the volatile-rich substrate, it could alternatively have been controlled by the thickness of the interior lava. Since the lava thickness presumably increases toward the center of Rachmaninoff, flow thickness will be greater in the west of Suge Facula than in the east. The location of the western margin of Suge Facula might therefore reflect a threshold thickness of lava above which subsurface volatile loss did not manifest at the surface. Alternatively, as the supply of lava waned following the creation of an originally more extensive region of pitted ground, subsequent lava flows emanating sources within the Rachmaninoff peak ring might not have reached as far as the proposed flow terminus at the eastern margin of Suge Facula, but were of sufficient thickness to bury any pitted ground texture that developed west of Suge Facula. In any case, the occurrence of pitted ground within impact craters, rather than in Mercury's major regions of smooth plains suggests that relatively small-volume effusive eruptions, such as those that took place in craters postdating the cessation of large-volume plains volcanism on Mercury, are required for pitted ground texture to be preserved.

Rustaveli's peak ring (Fig. 11b) is almost entirely surrounded and embayed by smooth plains, with only the tops of presumably the largest

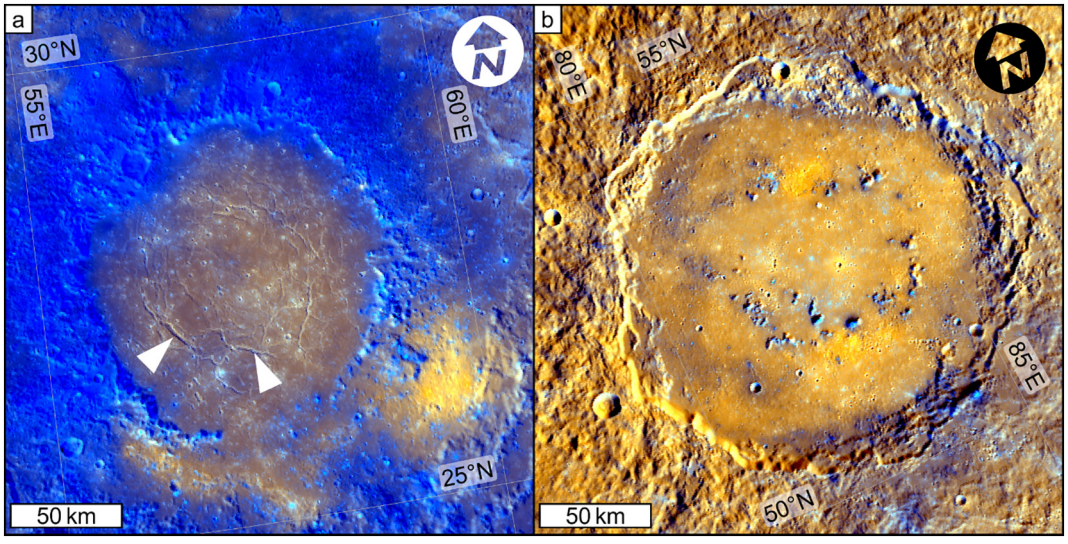

Fig. 11. Examples of post-impact volcanism in H05. (a) The interior of Rachmaninoff basin in ~665 m/pixel enhanced color (see wider view in Fig. 5c). Smooth, high-reflectance spectrally "red" plains, which exhibit concentric grabens (two larger examples indicated by white arrows), are situated within Rachmaninoff's peak ring. These plains have breached the peak ring in the south. The spectrally bright spot in the lower-right of the image is Suge Facula, an is an example of Mercury's pitted ground (Thomas et al., 2014a). More minor pitted ground faculae occur at the terminus of the high-reflectance red plains at the bottom of the image (see labelling in Fig. 12). (b) Rustaveli basin in ~665 m/pixel enhanced color. The smooth plains on Rustaveli's floor almost completely bury the crater's peak ring. Pitted ground faculae are located around the peak ring elements protruding through the later smooth plains. Both panels show the default LCC projection of H05.

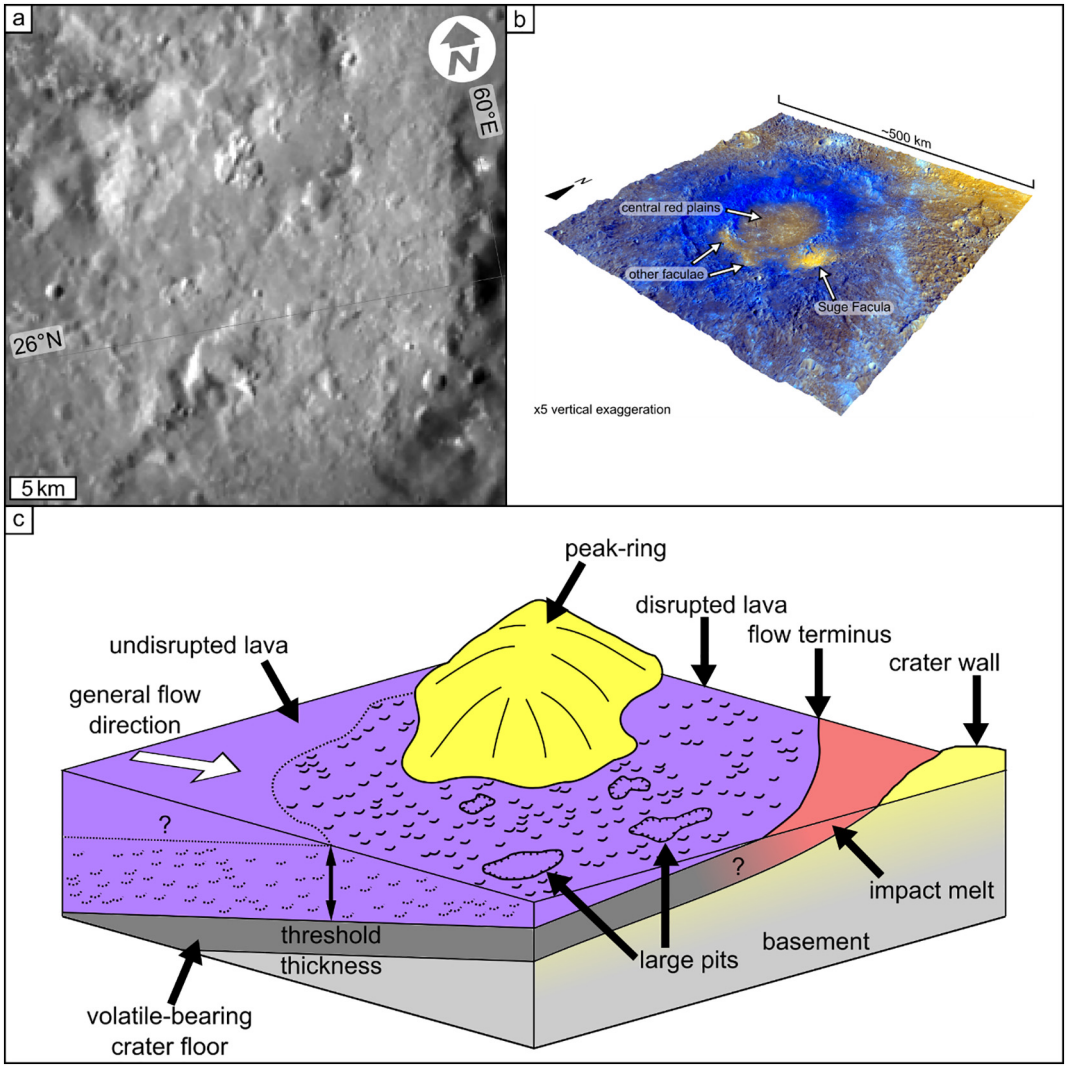

Fig. 12. Pitted ground in Rachmaninoff. (a) A close-up of the pitted texture of Suge Facula. (b) A perspective view of Rachmaninoff made using the 222 m/pixel DEM of H05 (Stark et al., 2017) overlain by the 665 m/pixel enhanced color MDIS mosaic. This view shows the same approximate perspective as the schematic in (c). (c) Schematic showing how pitted ground forms when lava flows over a volatile bearing substrate, but that a sufficiently thick lava could bury this texture. After Wright et al. (2019).

mountain peaks protruding from the plains. Burial of the peak ring of a crater of this size cannot be achieved by the anticipated thickness of impact melt alone (Grieve and Cintala, 1992; Cintala and Grieve, 1998), supporting the view that this basin, too, hosts post-impact volcanic smooth plains.

Several studies of Mercury's record of explosive volcanism show that vents and faculae are commonly co-located with impact craters (Kerber et al., 2011; Goudge et al., 2014; Thomas et al., 2014b; Jozwiak et al., 2018). Indeed, it appears that impact cratering has a statistically robust spatial control on the occurrence of explosive volcanism on Mercury (Klimczak et al., 2018). Furthermore, most (>70%) of putative explosive volcanic vents on Mercury are compound, meaning they were formed by multiple eruptions occurring at essentially the same place (Pegg et al., 2021). This observation supports the view that structurally controlled magma ascent pathways, once established, were continuously utilized by ascending magma because the stress required to keep those conduits open would have been less than that need to form new fractures in the crust—especially under a horizontally compressive tectonic stress state. Therefore, the fractures propagated by impact cratering likely played a key role in enabling the ascent and eruption of magmas on Mercury after the onset of global contraction (Byrne, 2020).

Several vents and faculae are located within the periphery of Caloris Planitia, but none is found more than 100 km inside it (Head et al., 2008; Rothery et al., 2014; Jozwiak et al., 2018). This arrangement resembles the occurrence of post-mare-volcanism on the Moon around the edges of the lunar mare basins (McGovern and Litherland, 2011). It is possible that the quasi-circular lithospheric loads represented by the lunar mare cause lithospheric flexure such that an annulus surrounding the load undergoes extension: such a stress state is favourable for magma ascent around this periphery and so could be responsible for localising small-volume, late-stage lunar volcanism around the edges of lunar mare basins (McGovern and Litherland, 2011). This same process might explain the occurrence of several volcanic vents near the edge of Caloris Planitia (Byrne et al., 2018a). In addition, it might explain the occurrence of Nathair Facula, Neidr Facula, and other smaller putative pyroclastic deposits in H05, along the southern margin of Borealis Planitia (Wright, 2019).

2.3.2. Lobate scarps

Some studies have postulated that faults might act as pre-existing weaknesses that ascending magmas could exploit to reach the surface (Klimczak et al., 2013; Thomas et al., 2015). There are some examples of small patches of smooth plains embaying lobate scarps (Fig. 8:

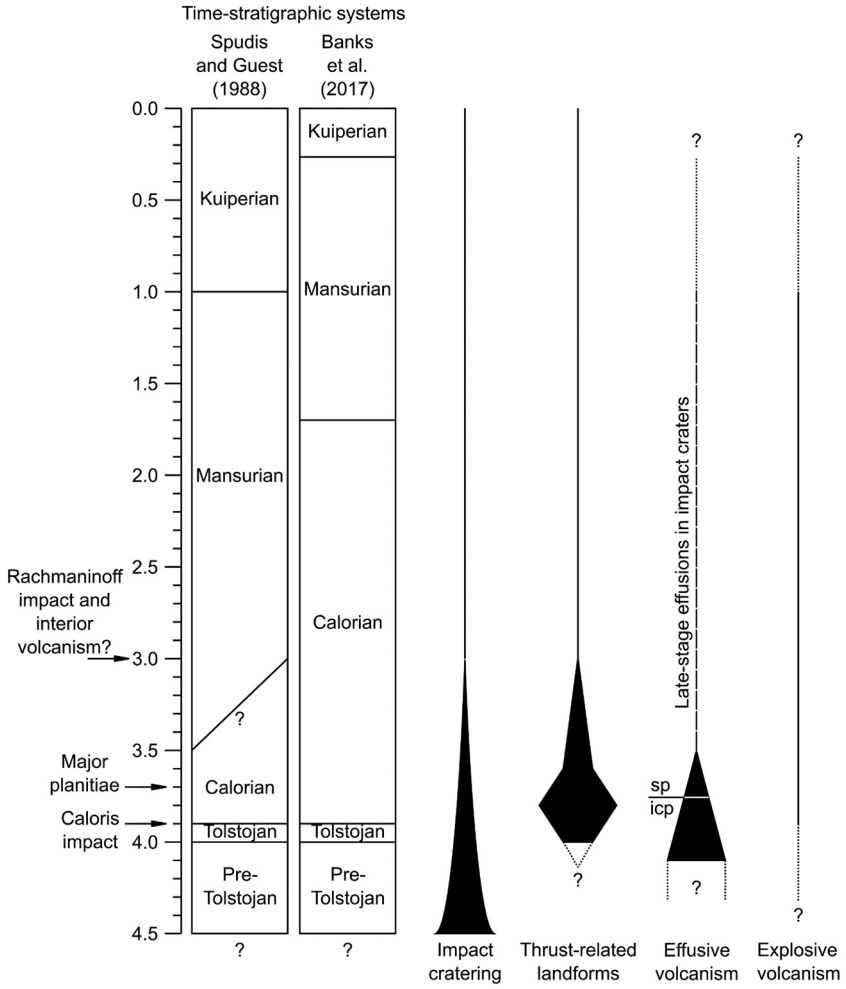

Fig. 13. Graphical summary of the geological history of Mercury. An absolute model timescale is shown at the left. The shapes on the right are schematic representations of the relative intensity and duration of key geological processes on Mercury discussed in this paper. Absolute model ages of relevant geological events are shown at the left. The horizontal line separating the labels "sp" (smooth plains) and "icp" (intercrater plains) indicates the approximate time when plains volcanism changed from being preserved as intercrater plains to smooth plains. Question marks indicate uncertainties about the timings and durations of geological processes.

Malliband et al., 2018). These ponded patches could correspond to localized, late-stage effusions, presumably erupted via fractures kinematically associated with the scarp-producing thrusts, but in some cases an ejecta origin for these plains cannot be ruled out. Some workers observed that explosive vents and lobate scarps are closely spatially collocated (Thomas et al., 2014b), although others argued that they are generally not (Jozwiak et al., 2018). Klimczak et al. (2018) statistically tested the spatial association between lobate scarps and pyroclastic vents. These authors found that shortening structures on Mercury are so widespread that, although there is an apparent spatial association between shortening structures and vents, it is statistically equivocal given the relatively high probability that this co-location could have arisen by chance alone (Klimczak et al., 2018).

2.4. Influence of volcanism on tectonism

Mercury's tectonic expression also appears to have been influenced by its volcanic characteristics in some cases. For example, major fault systems partially border a region with relatively high Mg abundances in the Victoria quadrangle, to the west of H05 (Galluzzi et al., 2019). Morphologically, this "high-Mg region" constitutes intercrater plains (Galluzzi et al., 2016), and thus the surface rocks are probably the remains of lavas erupted early in Mercury's history (Whitten et al., 2014). High-Mg magmas form by high degrees of partial melting of undepleted mantle (Charlier et al., 2013). Therefore, it is possible that these high-Mg lavas erupted due to high degrees of partial melting extracted from a chemically heterogeneous mantle (Frank et al., 2017). The interior of the high-Mg region has a far lower spatial density of faulting than its edges, and thus it is possible that this region constitutes a mechanically strong crustal block that focused crustal shortening along its edges (Galluzzi et al., 2019).

Mercury's volcanic smooth plains probably represent a more competent surface unit than the intercrater plains, and this strength contrast has effected some control on the expression of Mercury's tectonics (Byrne et al., 2014). For example, as stated previously, there is relatively spatially restricted extensional tectonism on Mercury (Byrne et al., 2018a). However, networks of grabens are found within some volcanic plains inside impact craters, such as Rachmaninoff (Fig. 11a: Blair et al., 2013), or ghost craters such as Copland (Freed et al., 2012). Here, the impact crater may have "shielded" the internal volcanic plains from Mercury's prevailing stress regime, possibly through strain partitioning into the perimeter of the impact feature itself. This partitioning might have permitted the interior plains to contract thermally causing "thin-skinned" extensional faulting within such volcanic units of sufficient thickness (Freed et al., 2012; Blair et al., 2013). Some volcanic fills in larger basins have lobate scarps concentrated at their edges, which perhaps formed when the interface between the strong volcanic infill and the basin floor acted as a décollement that restricted shortening strain to the edge of the volcanic fill (Fegan et al., 2017).

3. Summary

Mercury's planetary evolution is summarised in Fig. 13. Impact cratering was a presumably a dominant process in Mercury's early history, and, though greatly diminished, continues into the present. The oldest surfaces on Mercury formed ~4.1 Ga, probably by a combination of effusive volcanism and basin formation (Marchi et al., 2013). Effusive volcanism possibly occurred before then, but no record of that time remains. Continual effusive volcanism (4.1–3.75 Ga) is recorded by intercrater plains (Whitten et al., 2014), and subsequently large-volume smooth plains (3.75–3.5 Ga: Head et al., 2011; Denevi et al., 2013; Ostrach et al., 2015; Byrne et al., 2016). Small-volume effusive volcanism occurred sporadically in impact craters (Prockter et al., 2010; Blair et al., 2013; Fegan et al., 2017; Wright et al., 2018) for an uncertain duration following the cessation of large-volume eruptions. Explosive volcanism persisted throughout much of Mercury's history, but when this process began remains mysterious (Thomas et al., 2014b; Jozwiak et al., 2018). While large-volume effusive volcanism was coming to an end, the largest thrust-fault-related landforms formed in response to Mercury's global contraction (Byrne et al., 2014; Banks et al., 2015; Giacomini et al., 2020). There is evidence that small-scale thrust faulting continued into Mercury's recent geological history (Watters et al., 2016). Thus, Mercury's geological evolution has been dominated by a widespread horizontally compressive stress regime imposed by global contraction in response to secular cooling of the planet's interior. The Hokusai quadrangle represents a useful site on Mercury in which to examine the interplay between tectonic and volcanic activity before, during, and after the innermost planet transitioned into a state of global contraction.

Lower-volume flows that form the intermediate plains in H05 could represent the terminal smooth plains volcanism if they formed similarly to the graded terrain of Byrne et al. (2013), but the stratigraphic relationship between Borealis Planitia smooth plains and the intermediate plains remains uncertain. After global contraction caused the cessation of large-volume effusive volcanism on Mercury, impact craters such as Rachmaninoff and Rustaveli hosted relatively minor effusions that allowed the preservation of the small but compositionally distinct pitted ground. There might also have been late-stage, small-volume effusive eruptions that took advantage of fractures associated with lobate scarps (Malliband et al., 2018). The intermediate plains, pitted ground, and small ponds of smooth plains against lobate scarps in H05, and elsewhere, are key targets for the BepiColombo mission to Mercury (Rothery et al., 2020a), with which we might understand further the interwoven history of volcanism and tectonism on the innermost planet.

Declaration of Competing Interest

The authors declare that they have no known competing financial interests or personal relationships that could have appeared to influence the work reported in this paper.

Acknowledgements

The planetary data products used in this work are publicly available from the Planetary Data System (PDS). MESSENGER data are credited to NASA/Johns Hopkins University Applied Physics Laboratory/Carnegie Institute of Washington. J. Wright was funded by a postgraduate studentship grant (ST/N50421X/1) from the UK Science and Technology Facilities Council (STFC) during the early stages of research for this manuscript. J. Wright and D. A. Rothery were funded by PLANMAP during the final data collection, analysis, and write-up of this manuscript. This project has received funding from the European Union's Horizon 2020 research and innovation programme under grant agreement No. 776276. J. Wright is grateful to B. W. Denevi for providing the smooth plains shapefile used in Fig. 4, and to F. E. G. Butcher for helping with CraterStats2. The authors are grateful to an anonymous reviewer, whose suggestions substantially improved the manuscript.

Appendix A. Supplementary data

Supplementary data to this article can be found online at https://doi.org/10.1016/j.jvolgeores.2021.107300.

References

Banks, M.E., Xiao, Z., Watters, T.R., Strom, R.G., Braden, S.E., Chapman, C.R., Solomon, S.C., Klimczak, C., Byrne, P.K., 2015. Duration of activity on lobate-scarp thrust faults on Mercury. J. Geophys. Res. Planets 120, 1751–1752. https://doi.org/10.1002/2015JE004828.

Banks, M.E., Xiao, Z., Braden, S.E., Barlow, N.G., Chapman, C.R., Fassett, C.I., Marchi, S.S., 2017. Revised constraints on absolute age limits for Mercury's Kuiperian and Mansurian stratigraphic systems. J. Geophys. Res. Planets 122, 1010–1020. https://doi.org/10.1002/2016JE005254.

Becker, K.J., Robinson, M.S., Becker, T.L., Weller, L.A., Edmundson, K.L., Neumann, G.A., Perry, M.E., Solomon, S.C., 2016. First global digital elevation model of Mercury. 47th Lunar and Planetary Science Conference (The Woodlands, Houston, p. Abstract #2959).

Benkhoff, J., van Casteren, J., Hayakawa, H., Fujimoto, M., Laakso, H., Novara, M., Ferri, P., Middleton, H.R., Ziethe, R., 2010. BepiColombo—Comprehensive exploration of Mercury: mission overview and science goals. Planet. Space Sci. 58, 2–20. https://doi.org/10.1016/j.pss.2009.09.020.

Beuthe, M., 2010. East-west faults due to planetary contraction. Icarus 209, 795–817. https://doi.org/10.1016/j.icarus.2010.04.019.

Blair, D.M., Freed, A.M., Byrne, P.K., Klimczak, C., Prockter, L.M., Ernst, C.M., Solomon, S.C., Melosh, H.J., Zuber, M.T., 2013. The origin of graben and ridges in Rachmaninoff, Raditladi, and Mozart basins, Mercury. J. Geophys. Res. Planets 118, 47–58. https://doi.org/10.1029/2012JE004198.

Blewett, D.T., Robinson, M.S., Denevi, B.W., Gillis-Davis, J.J., Head, J.W., Solomon, S.C., Holsclaw, G.M., McClintock, W.E., 2009. Multispectral images of Mercury from the first MESSENGER flyby: analysis of global and regional color trends. Earth Planet. Sci. Lett. 285, 272–282. https://doi.org/10.1016/j.epsl.2009.02.021.

Brož, P., Hauber, E., 2012. A unique volcanic field in Tharsis, Mars: pyroclastic cones as evidence for explosive eruptions. Icarus 218, 88–99. https://doi.org/10.1016/j.icarus.2011.11.030.

Brož, P., Čadek, O., Wright, J., Rothery, D.A., 2018. The apparent absence of kilometer-sized pyroclastic volcanoes on Mercury: are we looking right? Geophys. Res. Lett. 45, 12171–12179. https://doi.org/10.1029/2018GL079902.

Byrne, P.K., Klimczak, C., Williams, D.A., Hurwitz, D.M., Solomon, S.C., Head, J.W., Preusker, F., Oberst, J., 2013. An assemblage of lava flow features on Mercury. J. Geophys. Res. Planets 118, 1303–1322. https://doi.org/10.1002/jgre.20052.

Byrne, P.K., Klimczak, C., Şengör, A..M.C., Solomon, S.C., Watters, T.R., Hauck, S.A., 2014. Mercury's global contraction much greater than earlier estimates. Nat. Geosci. 7, 301–307. https://doi.org/10.1038/ngeo2097.

Byrne, P.K., Ostrach, L.R., Fassett, C.I., Chapman, C.R., Denevi, B.W., Evans, A.J., Klimczak, C., Banks, M.E., Head, J.W., Solomon, S.C., 2016. Widespread effusive volcanism on Mercury likely ended by about 3.5 Ga. Geophys. Res. Lett. 43, 7408–7416. https://doi.org/10.1002/2016GL069412.

Byrne, P.K., 2020. A comparison of inner Solar System volcanism. Nat. Astron. 4, 321–327. https://doi.org/10.1038/s41550-019-0944-3.

Byrne, P.K., Klimczak, C., Şengör, A..M.C., 2018a. The Tectonic character of Mercury. In: Solomon, S.C., Nittler, L.R., Anderson, B.J. (Eds.), Mercury: the View after MESSENGER. Cambridge University Press, Cambridge, pp. 249–286 https://doi.org/10.1017/9781316650684.011.

Byrne, P.K., Whitten, J.L., Klimczak, C., McCubbin, F.M., Ostrach, L.R., 2018b. The Volcanic character of Mercury. In: Solomon, S.C., Nittler, L.R., Anderson, B.J. (Eds.), Mercury: the View after MESSENGER. Cambridge University Press, Cambridge, pp. 287–323 https://doi.org/10.1017/9781316650684.012.

Cashman, K.V., 2004. Volatile controls on magma ascent and eruption. In: Sparks, R.S.J., Hawkesworth, C.J. (Eds.), The State of the Planet: Frontiers and Challenges in Geophysics, pp. 109–124 https://doi.org/10.1029/150GM10.

Cavanaugh, J.F., Smith, J.C., Sun, X., Bartels, A.E., Ramos-Izquierdo, L., Krebs, D.J., McGarry, J.F., Trunzo, R., Novo-Gradac, A.M., Britt, J.L., Karsh, J., Katz, R.B., Lukemire, A.T., Szymkiewicz, R., Berry, D.L., Swinski, J.P., Neumann, G.A., Zuber, M.T., Smith, D.E., 2007. The Mercury laser altimeter instrument for the MESSENGER mission. Space Sci. Rev. 131, 451–479. https://doi.org/10.1007/s11214-007-9273-4.

Chapman, C.R., Merline, W.J., Marchi, S., Prockter, L.M., Fassett, C.I., Head, J.W., Solomon, S.C., Xiao, Z., 2012. The young inner plains of Mercury's Rachmaninoff basin reconsidered. 43rd Lunar and Planetary Science Conference (The Woodlands, Houston, p. Abstract #1607).

Charlier, B., Grove, T.L., Zuber, M.T., 2013. Phase equilibria of ultramafic compositions on Mercury and the origin of the compositional dichotomy. Earth Planet. Sci. Lett. 363, 50–60. https://doi.org/10.1016/j.epsl.2012.12.021.

Cintala, M.J., Grieve, R.A.F., 1998. Scaling impact melting and crater dimensions: implications for the lunar cratering record. Meteorit. Planet. Sci. 33, 889–912. https://doi.org/10.1111/j.1945-5100.1998.tb01695.x.

Davies, M.E., Dornik, S.E., Gault, D.E., Strom, R.G., 1978. Atlas of Mercury. NASA Special Publication.

Davison, T.M., Ciesla, F.J., Collins, G.S., 2012. Post-impact thermal evolution of porous planetesimals. Geochim. Cosmochim. Acta 95, 252–269. https://doi.org/10.1016/j.gca.2012.08.001.

Denevi, B.W., Ernst, C.M., Meyer, H.M., Robinson, M.S., Murchie, S.L., Whitten, J.L., Head, J.W., Watters, T.R., Solomon, S.C., Ostrach, L.R., Chapman, C.R., Byrne, P.K., Klimczak, C., Peplowski, P.N., 2013. The distribution and origin of smooth plains on Mercury. J. Geophys. Res. Planets 118, 891–907. https://doi.org/10.1002/jgre.20075.

Dombard, A.J., Hauck, S.A., 2008. Despinning plus global contraction and the orientation of lobate scarps on Mercury: predictions for MESSENGER. Icarus 198, 274–276. https://doi.org/10.1016/j.icarus.2008.06.008.

Dunne, J.A., Burgess, E., 1978. The Voyage of Mariner 10. NASA Special Publication.

Ebel, D.S., Stewart, S.T., 2018. The elusive origin of Mercury. In: Solomon, S.C., Nittler, L.R., Anderson, B.J. (Eds.), Mercury: the View after MESSENGER. Cambridge University Press, Cambridge, pp. 497–515 https://doi.org/10.1017/9781316650684.019.

Eggleton, R.E., Schaber, G.G., 1972. Photogeology: Part B: Cayley Formation interpreted as basin ejecta. Apollo 16 Preliminary Science Report (NASA SP 315) (Washington D.C., pp. 29–7–29–16).

Elkins-Tanton, L.T., Hager, B.H., 2005. Giant meteoroid impacts can cause volcanism. Earth Planet. Sci. Lett. 239, 219–232. https://doi.org/10.1016/j.epsl.2005.07.029.

Evans, L.G., Peplowski, P.N., Rhodes, E.A., Lawrence, D.J., McCoy, T.J., Nittler, L.R., Solomon, S.C., Sprague, A.L., Stockstill-Cahill, K.R., Starr, R.D., Weider, S.Z., Boynton, W.V., Hamara, D.K., Goldsten, J.O., 2012. Major-element abundances on the surface of Mercury: results from the MESSENGER gamma-ray spectrometer. J. Geophys. Res. 117, 1–14. https://doi.org/10.1029/2012JE004178.

Fassett, C.I., Head, J.W., Blewett, D.T., Chapman, C.R., Dickson, J.L., Murchie, S.L., Solomon, S.C., Watters, T.R., 2009. Caloris impact basin: Exterior geomorphology, stratigraphy, morphometry, radial sculpture, and smooth plains deposits. Earth Planet. Sci. Lett. 285, 297–308. https://doi.org/10.1016/j.epsl.2009.05.022.

Fedorenko, V., Czamanske, G., Zen'ko, T., Budahn, J., Siems, D., 2000. Field and geochemical studies of the melilite-bearing Arydzhangsky suite, and an overall perspective on the Siberian alkaline-ultramafic flood-volcanic rocks. Int. Geol. Rev. 42, 769–804. https://doi.org/10.1080/00206810009465111.

Fegan, E.R., Rothery, D.A., Marchi, S.S., Massironi, M., Conway, S.J., Anand, M., 2017. Late movement of basin-edge lobate scarps on Mercury. Icarus 288, 226–234. https://doi.org/10.1016/j.icarus.2017.01.005.

Frank, E.A., Potter, R.W.K., Abramov, O., James, P.B., Klima, R.L., Mojzsis, S.J., Nittler, L.R., 2017. Evaluating an impact origin for Mercury's high-magnesium region. J. Geophys. Res. Planets 122, 614–632. https://doi.org/10.1002/2016JE005244.

Freed, A.M., Blair, D.M., Watters, T.R., Klimczak, C., Byrne, P.K., Solomon, S.C., Zuber, M.T., Melosh, H.J., 2012. On the origin of graben and ridges within and near volcanically buried craters and basins in Mercury's northern plains. J. Geophys. Res. Planets 117, E00L06. https://doi.org/10.1029/2012JE004119.

Galluzzi, V., Guzzetta, L., Ferranti, F., Di Achille, G., Rothery, D.A., Palumbo, P., 2016. Geology of the Victoria quadrangle (H02), Mercury. J. Maps 12, 227–238. https://doi.org/10.1080/17445647.2016.1193777.

Galluzzi, V., Ferranti, L., Massironi, M., Giacomini, L., Guzzetta, L., Palumbo, P., 2019. Structural analysis of the Victoria quadrangle fault systems on Mercury: timing, geometries, kinematics, and relationship with the high-Mg Region. J. Geophys. Res. Planets 124, 2543–2562. https://doi.org/10.1029/2019JE005953.

Giacomini, L., Massironi, M., Marchi, S., Fassett, C.I., Di Achille, G., Cremonese, G., 2015. Age dating of an extensive thrust system on Mercury: Implications for the planet's thermal evolution. In: Platz, T., Massironi, M., Byrne, P.K., Hiesinger, H. (Eds.), Volcanism and Tectonism Across the Inner Solar System. Geological Society of London, pp. 291–311 https://doi.org/10.1144/SP401.21.

Giacomini, L., Massironi, M., Galluzzi, V., Ferrari, S., Palumbo, P., 2020. Dating long thrust systems on Mercury: new clues on the thermal evolution of the planet. Geosci. Front. 11, 855–870. https://doi.org/10.1016/j.gsf.2019.09.005.

Goldsten, J.O., Rhodes, E.A., Boynton, W.V., Feldman, W.C., Lawrence, D.J., Trombka, J.I., Smith, D.M., Evans, L.G., White, J., Madden, N.W., Berg, P.C., Murphy, G.A., Gurnee, R.S., Strohbehn, K., Williams, B.D., Schaefer, E.D., Monaco, C.A., Cork, C.P., Del Eckels, J., Miller, W.O., Burks, M.T., Hagler, L.B., DeTeresa, S.J., Witte, M.C., 2007. The MESSENGER Gamma-Ray and Neutron Spectrometer. In: Domingue, D.L., Russell, C.T. (Eds.), The Messenger Mission to Mercury. Springer, New York, NY, pp. 339–391 https://doi.org/10.1007/978-0-387-77214-1_10.

Goudge, T.A., Head, J.W., Kerber, L., Blewett, D.T., Denevi, B.W., Domingue, D.L., Gillis-Davis, J.J., Gwinner, K., Helbert, J., Holsclaw, G.M., Izenberg, N.R., Klima, R.L., McClintock, W.E., Murchie, S.L., Neumann, G.A., Smith, D.E., Strom, R.G., Xiao, Z., Zuber, M.T., Solomon, S.C., 2014. Global inventory and characterisation of pyroclastic deposits on Mercury: new insights into pyroclastic activity from MESSENGER orbital data. J. Geophys. Res. Planets 119, 635–658. https://doi.org/10.1002/2013JE004480.

Grieve, R.A.F., Cintala, M.J., 1992. An analysis of differential impact melt-crater scaling and implications for the terrestrial impact record. Meteoritics 27, 526–538. https://doi.org/10.1111/j.1945-5100.1992.tb01074.x.

Guzzetta, L., Galluzzi, V., Ferranti, L., Palumbo, P., 2017. Geology of the Shakespeare quadrangle (H03), Mercury. J. Maps 13, 227–238. https://doi.org/10.1080/17445647.2017.1290556.

Hawkins, S.E., Boldt, J.D., Darlington, E.H., Espiritu, R., Gold, R.E., Gotwols, B., Grey, M.P., Hash, C.D., Hayes, J.R., Jaskulek, S.E., Kardian, C.J., Keller, M.R., Malaret, E.R., Murchie, S.L., Murphy, P.K., Peacock, K., Prockter, L.M., Reiter, R.A., Robinson, M.S., Schaefer, E.D., Shelton, R.G., Sterner, R.E., Taylor, H.W., Watters, T.R., Williams, B.D., 2007. The Mercury dual imaging system on the MESSENGER spacecraft. Space Sci. Rev. 131, 247–338. https://doi.org/10.1007/s11214-007-9266-3.

Head, J.W., Murchie, S.L., Prockter, L.M., Robinson, M.S., Solomon, S.C., Strom, R.G., Chapman, C.R., Watters, T.R., McClintock, W.E., Blewett, D.T., Gillis-Davis, J.J., 2008. Volcanism on Mercury: evidence from the first MESSENGER flyby. Science 321 (80), 69–72. https://doi.org/10.1126/science.1159256.

Head, J.W., Chapman, C.R., Strom, R.G., Fassett, C.I., Denevi, B.W., Blewett, D.T., Ernst, C.M., Watters, T.R., Solomon, S.C., Murchie, S.L., Prockter, L.M., Chabot, N.L., Gillis-Davis, J.J., Whitten, J.L., Goudge, T.A., Baker, D.M.H., Hurwitz, D.M., Ostrach, L.R., Xiao, Z., Merline, W.J., Kerber, L., Dickson, J.L., Oberst, J., Byrne, P.K., Klimczak, C., Nittler, L.R., 2011. Flood volcanism in the northern high latitudes of Mercury revealed by MESSENGER. Science 333 (80), 1853–1856. https://doi.org/10.1126/science.1211997.

Ivanov, B.A., Melosh, H.J., 2003. Impacts do not initiate volcanic eruptions: eruptions close to the crater. Geology 31, 869–872. https://doi.org/10.1130/G19669.1.

James, P.B., 2018. The enigma of Mercury's northern rise. Mercury: Current and Future Science of the Innermost Planet (p. Abstract #6053).

Jozwiak, L.M., Head, J.W., Wilson, L., 2018. Explosive volcanism on Mercury: analysis of vent and deposit morphology and modes of eruption. Icarus 302, 191–212. https://doi.org/10.1016/j.icarus.2017.11.011.

Kerber, L., Head, J.W., Solomon, S.C., Murchie, S.L., Blewett, D.T., Wilson, L., 2009. Explosive volcanic eruptions on Mercury: eruption conditions, magma volatile content, and implications for interior volatile abundances. Earth Planet. Sci. Lett. 285, 263–271. https://doi.org/10.1016/j.epsl.2009.04.037.

Kerber, L., Head, J.W., Blewett, D.T., Solomon, S.C., Wilson, L., Murchie, S.L., Robinson, M.S., Denevi, B.W., Domingue, D.L., 2011. The global distribution of pyroclastic deposits on Mercury: the view from MESSENGER flybys 1–3. Planet. Space Sci. 59, 1895–1909. https://doi.org/10.1016/j.pss.2011.03.020.

Kinczyk, M.J., Prockter, L.M., Byrne, P.K., Susorney, H.C.M., Chapman, C.R., 2020. A morphological evaluation of crater degradation on Mercury: revisiting crater classification with MESSENGER data. Icarus 341, 113637. https://doi.org/10.1016/j.icarus.2020.113637.

Klimczak, C., 2015. Limits on the brittle strength of planetary lithospheres undergoing global contraction. J. Geophys. Res. Planets 120, 2135–2151. https://doi.org/10.1002/2015JE004851.

Klimczak, C., Byrne, P.K., Solomon, S.C., Nimmo, F., Watters, T.R., Denevi, B.W., Ernst, C.M., Maria, E., Observatory, L.E., 2013. The role of thrust faults as conduits for volatiles on Mercury. Lunar and Planetary Science Conference (p. Abstract #1390).

Klimczak, C., Crane, K.T., Habermann, M.A., Byrne, P.K., 2018. The spatial distribution of Mercury's pyroclastic activity and the relation to lithospheric weaknesses. Icarus 315, 115–123. https://doi.org/10.1016/j.icarus.2018.06.020.

Klimczak, C., Byrne, P.K., Celâl Şengör, A.M., Solomon, S.C., 2019. Principles of structural geology on rocky planets. Can. J. Earth Sci. 56, 1437–1457. https://doi.org/10.1139/cjes-2019-0065.

Kreslavsky, M.A., Head, J.W., 2015. A thicker regolith on Mercury. 46th Lunar and Planetary Science Conference (The Woodlands, Houston, p. #1246).

Lawrence, S.J., Stopar, J.D., Hawke, B.R., Greenhagen, B.T., Cahill, J.T.S., Bandfield, J.L., Jolliff, B.L., Denevi, B.W., Robinson, M.S., Glotch, T.D., Bussey, D.B.J., Spudis, P.D., Giguere, T.A., Garry, W.B., 2013. LRO observations of morphology and surface roughness of volcanic cones and lobate lava flows in the Marius Hills. J. Geophys. Res. Planets 118, 615–634. https://doi.org/10.1002/jgre.20060.

Le Feuvre, M., Wieczorek, M.A., 2011. Nonuniform cratering of the Moon and a revised crater chronology of the inner Solar System. Icarus 214, 1–20. https://doi.org/10.1016/j.icarus.2011.03.010.

Lorenz, V., 1986. On the growth of maars and diatremes and its relevance to the formation of tuff rings. Bull. Volcanol. 48, 265–274. https://doi.org/10.1007/BF01081755.

Malliband, C.C., Rothery, D.A., Balme, M.R., Conway, S.J., 2018. Small smooth units ("young" lavas?) abutting lobate scarps on Mercury. Mercury: Current and Future Science of the Innermost Planet (Columbia, Maryland, p. Abstract #6092).

Mancinelli, P., Minelli, F., Pauselli, C., Federico, C., 2016. Geology of the Raditladi quadrangle, Mercury (H04). J. Maps 12, 190–202. https://doi.org/10.1080/17445647. 2016.1191384.

Marchi, S., Mottola, S., Cremonese, G., Massironi, M., Martellato, E., 2009. A new chronology for the Moon and Mercury. Astron. J. 137, 4936–4948. https://doi.org/10.1088/0004-6256/137/6/4936.

Marchi, S., Chapman, C.R., Fassett, C.I., Head, J.W., Bottke, W.F., Strom, R.G., 2013. Global resurfacing of Mercury 4.0-4.1 billion years ago by heavy bombardment and volcanism. Nature 499, 59–61. https://doi.org/10.1038/nature12280.

McCubbin, F.M., Riner, M.A., Vander Kaaden, K.E., Burkemper, L.K., 2012. Is Mercury a volatile-rich planet? Geophys. Res. Lett. 39, L09202. https://doi.org/10.1029/2012GL051711.

McGovern, P.J., Litherland, M.M., 2011. Lithospheric stress and basaltic magma ascent on the Moon, with implications for large volcanic provinces and edifices. 42nd Lunar and Planetary Science Conference https://doi.org/10.1038/NGEO897 (p. Abstract #2587).

Melosh, H.J., Dzurisin, D., 1978. Mercurian global tectonics: a consequence of tidal despinning? Icarus 35, 227–236. https://doi.org/10.1016/0019-1035(78)90007-6.

Menand, T., Daniels, K.A., Benghiat, P., 2010. Dyke propagation and sill formation in a compressive tectonic environment. J. Geophys. Res. Solid Earth 115, B08201. https://doi.org/10.1029/2009JB006791.

Michael, G.G., Neukum, G., 2010. Planetary surface dating from crater size-frequency distribution measurements: partial resurfacing events and statistical age uncertainty. Earth Planet. Sci. Lett. 294, 223–229. https://doi.org/10.1016/j.epsl.2009.12.041.

Michael, G.G., Platz, T., Kneissl, T., Schmedemann, N., 2012. Planetary surface dating from crater size-frequency distribution measurements: spatial randomness and clustering. Icarus 218, 169–177. https://doi.org/10.1016/j.icarus.2011.11.033.

Murchie, S.L., Watters, T.R., Robinson, M.S., Head, J.W., Strom, R.G., Chapman, C.R., Solomon, S.C., McClintock, W.E., Prockter, L.M., Domingue, D.L., Blewett, D.T., 2008. Geology of the Caloris basin, Mercury: a view from MESSENGER. Science 321 (80), 73–76. https://doi.org/10.1126/science.1159261.

Murray, B.C., Belton, M.J.S., Danielson, G.E., Davies, M.E., Gault, D.E., Hapke, B., O'Leary, B., Strom, R.G., Suomi, V., Trask, N.J., 1974. Mercury's surface: preliminary description and interpretation from Mariner 10 pictures. Science 185 (80), 169–179. https://doi.org/10.1126/science.185.4146.169.

Namur, O., Charlier, B., 2017. Silicate mineralogy at the surface of Mercury. Nat. Geosci. 10, 9–13. https://doi.org/10.1038/NGEO2860.
Neukum, G., Ivanov, B.A., Hartmann, W.K., 2001a. Cratering records in the inner solar system in relation to the lunar reference system. Space Sci. Rev. 96, 55–86. https://doi.org/10.1023/A:1011989004263.
Neukum, G., Oberst, J., Hoffmann, H., Wagner, R.J., Ivanov, B.A., 2001b. Geologic evolution and cratering history of Mercury. Planet. Space Sci. 49, 1507–1521. https://doi.org/10.1016/S0032-0633(01)00089-7.
Nittler, L.R., Starr, R.D., Weider, S.Z., McCoy, T.J., Boynton, W.V., Ebel, D.S., Ernst, C.M., Evans, L.G., Goldsten, J.O., Hamara, D.K., Lawrence, D.J., McNutt, R.L., Schlemm, C.E., Solomon, S.C., Sprague, A.L., 2011. The major-element composition of Mercury's surface from MESSENGER X-ray spectrometry. Science 333 (80), 1847–1850. https://doi.org/10.1126/science.1211567.
Nittler, L.R., Chabot, N.L., Grove, T.L., Peplowski, P.N., 2018. The chemical composition of Mercury. In: Solomon, S.C., Nittler, L.R., Anderson, B.J. (Eds.), Mercury: The View after MESSENGER. Cambridge University Press, Cambridge, pp. 30–51 https://doi.org/10.1017/9781316650684.003.
Nittler, L.R., Frank, E.A., Weider, S.Z., Crapster-Pregont, E., Vorburger, A., Starr, R.D., Solomon, S.C., 2020. Global major-element maps of Mercury from four years of MESSENGER X-Ray Spectrometer observations. Icarus 345, 113716. https://doi.org/10.1016/j.icarus.2020.113716.
Ostrach, L.R., Robinson, M.S., Whitten, J.L., Fassett, C.I., Strom, R.G., Head, J.W., Solomon, S.C., 2015. Extent, age, and resurfacing history of the northern smooth plains on Mercury from MESSENGER observations. Icarus 250, 602–622. https://doi.org/10.1016/j.icarus.2014.11.010.
Pegg, D.L., Rothery, D.A., Balme, M.R., Conway, S.J., 2021. Explosive vent sites on Mercury: Commonplace multiple eruptions and their implications. Icarus 365, 114510. https://doi.org/10.1016/j.icarus.2021.114510.
Peplowski, P.N., Lawrence, D.J., Rhodes, E.A., Sprague, A.L., McCoy, T.J., Denevi, B.W., Evans, L.G., Head, J.W., Nittler, L.R., Solomon, S.C., Stockstill-Cahill, K.R., Weider, S.Z., 2012. Variations in the abundances of potassium and thorium on the surface of Mercury: results from the MESSENGER Gamma-Ray Spectrometer. J. Geophys. Res. E Planet. 117, 1–27. https://doi.org/10.1029/2012JE004141.
Peplowski, P.N., Evans, L.G., Stockstill-Cahill, K.R., Lawrence, D.J., Goldsten, J.O., McCoy, T.J., Nittler, L.R., Solomon, S.C., Sprague, A.L., Starr, R.D., Weider, S.Z., 2014. Enhanced sodium abundance in Mercury's north polar region revealed by the MESSENGER Gamma-Ray Spectrometer. Icarus 228, 86–95. https://doi.org/10.1016/j.icarus.2013.09.007.
Peplowski, P.N., Klima, R.L., Lawrence, D.J., Ernst, C.M., Denevi, B.W., Frank, E.A., Goldsten, J.O., Murchie, S.L., Nittler, L.R., Solomon, S.C., 2016. Remote sensing evidence for an ancient carbon-bearing crust on Mercury. Nat. Geosci. 9, 273–276. https://doi.org/10.1038/ngeo2669.
Prockter, L.M., Ernst, C.M., Denevi, B.W., Chapman, C.R., Head, J.W., Fassett, C.I., Merline, W.J., Solomon, S.C., Watters, T.R., Strom, R.G., Cremonese, G., Marchi, S., Massironi, M., 2010. Evidence for young Volcanism on Mercury from the Third MESSENGER Flyby. Science 329 (80), 668–671. https://doi.org/10.1126/science.1188186.
Riedel, C., Ernst, G.G.J., Riley, M., 2003. Controls on the growth and geometry of pyroclastic constructs. J. Volcanol. Geotherm. Res. 127, 121–152. https://doi.org/10.1016/S0377-0273(03)00196-3.
Rothery, D.A., Thomas, R.J., Kerber, L., 2014. Prolonged eruptive history of a compound volcano on Mercury: volcanic and tectonic implications. Earth Planet. Sci. Lett. 385, 59–67. https://doi.org/10.1016/j.epsl.2013.10.023.
Rothery, D.A., Mancinelli, P., Guzzetta, L., Wright, J., 2017. Mercury's Caloris basin: continuity between the interior and exterior plains. J. Geophys. Res. Planets 122, 560–576. https://doi.org/10.1002/2017JE005282.
Rothery, D.A., Massironi, M., Alemanno, G., Barraud, O., Besse, S., Bott, N., Brunetto, R., Bunce, E., Byrne, P., Capaccioni, F., Capria, M.T., Carli, C., Charlier, B., Cornet, T., Cremonese, G., D'Amore, M., De Sanctis, M.C., Doressoundiram, A., Ferranti, L., Filacchione, G., Galluzzi, V., Giacomini, L., Grande, M., Guzzetta, L.G., Helbert, J., Heyner, D., Hiesinger, H., Hussmann, H., Hyodo, R., Kohout, T., Kozyrev, A., Litvak, M., Lucchetti, A., Malakhov, A., Malliband, C., Mancinelli, P., Martikainen, J., Martindale, A., Maturilli, A., Milillo, A., Mitrofanov, I., Mokrousov, M., Morlok, A., Muinonen, K., Namur, O., Owens, A., Nittler, L.R., Oliveira, J.S., Palumbo, P., Pajola, M., Pegg, D.L., Penttilä, A., Politi, R., Quarati, F., Re, C., Sanin, A., Schulz, R., Stangarone, C., Stojic, A., Tretiyakov, V., Väisänen, T., Varatharajan, I., Weber, I., Wright, J., Wurz, P., Zambon, F., 2020a. Rationale for BepiColombo studies of Mercury's surface and composition. Space Sci. Rev. 216, 66. https://doi.org/10.1007/s11214-020-00694-7.
Rothery, D.A., Barraud, O., Besse, S., Carli, C., Pegg, D., Wright, J., Zambon, F., 2021b. On the asymmetry of Nathair Facula, Mercury. Icarus 355, 114180. https://doi.org/10.1016/j.icarus.2020.114180 ISSN 0019-1035.
Schlemm, C.E., Starr, R.D., Ho, G.C., Bechtold, K.E., Hamilton, S.A., Boldt, J.D., Boynton, W.V., Bradley, W., Fraeman, M.E., Gold, R.E., Goldsten, J.O., Hayes, J.R., Jaskulek, S.E., Rossano, E., Rumpf, R.A., Schaefer, E.D., Strohbehn, K., Shelton, R.G., Thompson, R.E., Trombka, J.I., Williams, B.D., 2007. The X-ray Spectrometer on the MESSENGER Spacecraft. The Messenger Mission to Mercury. Springer, New York, NY, pp. 393–415 https://doi.org/10.1007/978-0-387-77214-1_11.
Sehlke, A., Whittington, A.G., 2015. Rheology of lava flows on Mercury: an analog experimental study. J. Geophys. Res. Planets 120, 1924–1955. https://doi.org/10.1002/2015JE004792.
Solomon, S.C., 1978. On volcanism and thermal tectonics on one-plate planets. Geophys. Res. Lett. 5, 461–464. https://doi.org/10.1029/GL005i006p00461.
Solomon, S.C., Head, J.W., 1980. Lunar Mascon Basins: Lava filling, tectonics, and evolution of the lithosphere. Rev. Geophys. Sp. Phys. 18, 107–141. https://doi.org/10.1029/RG018i001p00107.
Solomon, S.C., McNutt, R.L., Gold, R.E., Domingue, D.L., 2007. MESSENGER mission overview. Space Sci. Rev. 131, 3–39. https://doi.org/10.1007/s11214-007-9247-6.
Solomon, S.C., Nittler, L.R., Anderson, B.J., 2018. Mercury: the View after Messenger. Cambridge University Press, Cambridge https://doi.org/10.1017/9781316650684.
Spudis, P.D., Guest, J.E., 1988. Stratigraphy and geologic history of Mercury. In: Vilas, F., Chapman, C.R., Matthews, M.S. (Eds.), Mercury. University of Arizona Press, Tucson, pp. 118–164.
Stark, A., Preusker, F., Oberst, J., Matz, K.-D., Gwinner, K., Roatsch, T., 2017. High-resolution topography from MESSENGER orbital stereo imaging - the H5 quadrangle "Hokusai,". 48th Lunar and Planetary Science Conference (The Woodlands, Houston, p. Abstract #2287).
Strom, R.G., Neukum, G., 1988. The cratering record on mercury and the origin of impacting objects. In: Vilas, F., Chapman, C.R., Matthews, M.S. (Eds.), Mercury. University of Arizona Press, Tuscon, Arizona, pp. 336–373.
Strom, R.G., Chapman, C.R., Merline, W.J., Solomon, S.C., Head, J.W., 2008. Mercury cratering record viewed from MESSENGER's first flyby. Science 321 (80), 79–81. https://doi.org/10.1126/science.1159317.
Thomas, R.J., Rothery, D.A., Conway, S.J., Anand, M., 2014a. Mechanisms of explosive volcanism on Mercury: implications from its global distribution and morphology. J. Geophys. Res. Planets 119, 2239–2254. https://doi.org/10.1002/2014JE004692.
Thomas, R.J., Rothery, D.A., Conway, S.J., Anand, M., 2014b. Long-lived explosive volcanism on Mercury. Geophys. Res. Lett. 41, 6084–6092. https://doi.org/10.1002/2014GL061224.
Thomas, R.J., Rothery, D.A., Conway, S.J., Anand, M., 2014c. Hollows on Mercury: materials and mechanisms involved in their formation. Icarus 229, 221–235. https://doi.org/10.1016/j.icarus.2013.11.018.
Thomas, R.J., Rothery, D.A., Conway, S.J., Anand, M., 2015. Explosive volcanism in complex impact craters on Mercury and the Moon: influence of tectonic regime on depth of magmatic intrusion. Earth Planet. Sci. Lett. 431, 164–172. https://doi.org/10.1016/j.epsl.2015.09.029.
Trask, N.J., Guest, J.E., 1975. Preliminary geologic terrain map of Mercury. J. Geophys. Res. 80, 2461–2477. https://doi.org/10.1029/JB080i017p02461.
Vander Kaaden, K.E., McCubbin, F.M., 2016. The origin of boninites on Mercury: an experimental study of the northern volcanic plains lavas. Geochim. Cosmochim. Acta 173, 246–263. https://doi.org/10.1016/j.gca.2015.10.016.
Vander Kaaden, K.E., McCubbin, F.M., Nittler, L.R., Peplowski, P.N., Weider, S.Z., Frank, E.A., McCoy, T.J., 2017. Geochemistry, mineralogy, and petrology of boninitic and komatiitic rocks on the mercurian surface: insights into the mercurian mantle. Icarus 285, 155–168. https://doi.org/10.1016/j.icarus.2016.11.041.
Watters, T.R., Daud, K., Banks, M.E., Selvans, M.M., Chapman, C.R., Ernst, C.M., 2016. Recent tectonic activity on Mercury revealed by small thrust fault scarps. Nat. Geosci. 9, 743–747. https://doi.org/10.1038/ngeo2814.
Weider, S.Z., Nittler, L.R., Starr, R.D., McCoy, T.J., Stockstill-Cahill, K.R., Byrne, P.K., Denevi, B.W., Head, J.W., Solomon, S.C., 2012. Chemical heterogeneity on Mercury's surface revealed by the MESSENGER X-Ray Spectrometer. J. Geophys. Res. E Planet. 117, E00L05. https://doi.org/10.1029/2012JE004153.
Weider, S.Z., Nittler, L.R., Starr, R.D., Crapster-Pregont, E.J., Peplowski, P.N., Denevi, B.W., Head, J.W., Byrne, P.K., Hauck, S.A., Ebel, D.S., Solomon, S.C., 2015. Evidence for geochemical terranes on Mercury: global mapping of major elements with MESSENGER's X-Ray Spectrometer. Earth Planet. Sci. Lett. 416, 109–120. https://doi.org/10.1016/j.epsl.2015.01.023.
Weider, S.Z., Nittler, L.R., Murchie, S.L., Peplowski, P.N., McCoy, T.J., Kerber, L., Klimczak, C., Ernst, C.M., Goudge, T.A., Starr, R.D., Izenberg, N.R., Klima, R.L., Solomon, S.C., 2016. Evidence from MESSENGER for sulfur- and carbon-driven explosive volcanism on Mercury. Geophys. Res. Lett. 43, 3653–3661. https://doi.org/10.1002/2016GL068325.
Wetherill, G.W., 1994. Provenance of the terrestrial planets. Geochim. Cosmochim. Acta 58, 4513–4520. https://doi.org/10.1016/0016-7037(94)90352-2.
Whitten, J.L., Head, J.W., Denevi, B.W., Solomon, S.C., 2014. Intercrater plains on Mercury: Insights into unit definition, characterization, and origin from MESSENGER datasets. Icarus 241, 97–113. https://doi.org/10.1016/j.icarus.2014.06.013.
Wilhelms, D.E., 1976. Mercurian volcanism questioned. Icarus 28, 551–558. https://doi.org/10.1016/0019-1035(76)90128-7.
Wright, J., 2019. MESSENGER Observations of Volcanism on Mercury: From Hokusai Quadrangle Down to Small Cones. PhD thesis. The Open University https://doi.org/10.21954/ou.ro.0000f075.
Wright, J., Rothery, D.A., Balme, M.R., Conway, S.J., 2016. Preliminary observations of Rustaveli basin, Mercury. 47th Lunar and Planetary Science Conference (The Woodlands, Houston, p. Abstract #2063).
Wright, J., Rothery, D.A., Balme, M.R., Conway, S.J., 2018. Constructional Volcanic Edifices on Mercury: candidates and hypotheses of formation. J. Geophys. Res. Planets 123, 952–971. https://doi.org/10.1002/2017JE005450.
Wright, J., Rothery, D.A., Balme, M.R., Conway, S.J., 2019. Geology of the Hokusai quadrangle (H05). Mercury. J. Maps 15, 509–520. https://doi.org/10.1080/17445647.2019.1625821.
Zolotov, M.Y., Sprague, A.L., Hauck, S.A., Nittler, L.R., Solomon, S.C., Weider, S.Z., 2013. The redox state, FeO content, and origin of sulfur-rich magmas on Mercury. J. Geophys. Res. Planets 118, 138–146. https://doi.org/10.1029/2012JE004274.
Zuber, M.T., Smith, D.E., Phillips, R.J., Solomon, S.C., Neumann, G.A., Hauck, S.A., Peale, S.J., Barnouin, O.S., Head, J.W., Johnson, C.L., Lemoine, F.G., Mazarico, E., Sun, X., Torrence, M.H., Freed, A.M., Klimczak, C., Margot, J., Oberst, J., Perry, M.E., McNutt, R.L., Balcerski, J.A., Michel, N., Talpe, M.J., Yang, D., 2012. Topography of the Northern Hemisphere of Mercury from MESSENGER Laser Altimetry. Science 336 (80), 217–221. https://doi.org/10.1126/science.1218805.